LOW-FREQUENCY HYDROPHONE CALIBRATION USING ELASTIC WAVEGUIDES

by

Robert Drinnan

Submitted in partial fulfillment of the requirements
for the degree of Master of Science

at

Dalhousie University
Halifax, Nova Scotia
June 2023

To my father who inspired my passion for ocean science.

TABLE OF CONTENTS

LIST OF TABLES

LIST OF FIGURES

ABSTRACT

Modern hydrophone calibration techniques typically require sensors to be placed in a free field or within a hydrostatically varying chamber. Between 1 kHz and 10 kHz, the wavelength in water is too long for free-field conditions to be used in common tank sizes. A novel technique to calibrate hydrophones is investigated to address the measurement gap between very low-frequency and high-frequency techniques. Calibrations are performed in a 12-meter copper tube coiled into a 1-meter diameter helix. This elastic waveguide decreases the speed of sound within the apparatus, providing a longer reverb-free time for calibrations using a small volume. The propagation within the waveguide is studied with the deviations from the predicted theory discussed. Calibrations performed on Ocean Sonics icListen hydrophones are shown to be within 1 dB of independently calibrated reference measurements. This research demonstrates that using elastic waveguides is an effective and simple low-frequency hydrophone calibration method.

LIST OF ABBREVIATIONS AND SYMBOLS USED

Roman symbol	Description	Units
p	Pressure	Pa
c	Speed of sound	m/s
t	Time	s
m and n	Mode numbers	$\in\mathbb{Z}$
r	Pipe radial direction	m
z	Pipe axial direction	m
P	Lengendre polynomial	
J_n	nth Bessel function of the first kind	
Y_n	nth Bessel function of the second kind	
k	Principle wavenumber	1/m
q_{mn}	Wavenumber in the propagation axis	1/m
X_{nm}	Waveguide characteristic	
b	Pipe inner radius	m
d	Pipe outer radius	m
$\vec{u}$	Particle velocity	m/s
c_{nm}	Phase speed of n and mth mode	m/s
c_p	Phase speed	m/s
c_g	Group speed	m/s
c_c	Congressional speed	m/s
c_s	Shear speed	m/s
$\vec{S}$	Displacement	m
L	Lamé's First constant	
k_c	Congressional wavenumber	1/m
k_s	Shear wavenumber	1/m
P_m and T_m	Elastic solid characteristics	1/m
a	Radius of piston source	m

Roman symbol	Description	Units
$\tilde{b}$	Inner tube curvature	m
$\tilde{d}$	Outer tube curvature	m
$\tilde{q}$	Curved propagation wavenumber	rad/s
$\mathcal{R}$	Pipe helical radius	m
$\mathcal{C}$	Pipe helical circumference	m
C	Cross-correlation	
E_s	Energy of the signal	
T	Signal length	s
A	Signal amplitude	
s_{tr}	Transmitted signal	
$\hat{s_{tr}}$	Energy-normalized transmitted signal	
$\hat{C}$	Scaled cross-correlation	
E_{rc}	Received signal energy	V^2s
v_{rc}	Received signal voltage	V
PSD_{rc}	Received signal PSD	V
t_d	Time delay	s
P_r	Reference pressure	dB re μPa
$\mathcal{S}$	Hydrophone sensitivity	dB re V/μPa

Greek symbol	Description	Units
θ	Pipe polar direction	radians
ω	Angular frequency	rad/s
ω_c	Cutoff frequency	rad/s
Φ	Velocity potential	m^2/s
ρ_L	Density of liquid	kg/m^2
ρ_W	Density of pipe material	kg/m^2
ϕ	Time-independent velocity potential	m^2/s
Θ	Polar dependence function	
γ	Mode propagation angle	rad
σ_{rr}	Normal stress	Pa
σ_{rz}	Shear stress	Pa

Greek symbol	Description	Units
Ξ	Scalar displacement potential	m^2
Ψ	Vector displacement potential	m^2
μ	Shear modulus	Pa
ν	Poisson's ratio	

ACKNOWLEDGEMENTS

I am exceedingly grateful to Dr. David Barclay for his unwavering guidance throughout my research without which I could not have succeeded. Additionally, thank you to the rest of my committee, Dr. Jean-François Bousquet and Dr. Craig Brown, and the entire Noise lab for their enthusiastic support for my research.

Thank you to Ocean Sonics and Mitacs for their financial contributions to this project. I would like to acknowledge Jay Abel for providing the initial idea for this research. Finally, thank you to my family, especially Dr. Wayne Fulks, for helping me along the way.

CHAPTER 1

INTRODUCTION: A BRIEF HISTORY OF HYDROPHONE CALIBRATION

Hydrophones are crucial to the study of the ocean environment. Oceanographers and marine biologists use hydrophones to study all aspects of the ocean from monitoring marine wildlife to measuring and predicting seismic activity for earthquake monitoring. To ensure that measurements are reliable and accurate, hydrophones need to be calibrated. Hydrophone calibration at different frequencies has been a topic of research for the last 100 years. Sounds in the ocean are highly varied in frequency and each frequency band requires different techniques for proper calibration.

Historically, calibration was done by comparing the uncalibrated sensor's response to a known pressure source. While simple, this method had challenges in finding pressure sources of known amplitude across the multiple frequencies of interest to scientists and engineers. The requirement for previously calibrated pressure sources was removed with the introduction of reciprocity calibration by *MacLean* (1940). MacLean applied the principle of electroacoustic reciprocity to transducers in order to calibrate hydrophones without the need of a primary source. A reciprocal transducer is defined as one whose pressure generated from a fixed current is related to the voltage measured from receiving the same pressure. The key development was the introduction of the reciprocity parameter J which is defined as the ratio of received voltage sensitivity to transmitted current response. If the transducer is reciprocal (which is the case for most hydrophones) the reciprocity parameter is a function solely of the geometry of the system and not of the individual

transducer properties (*MacLean*, 1940). With multiple reciprocal transducers, using the reciprocity parameter for the system the calibration of all the test transducers can be determined without a primary source. MacLean derived the reciprocity parameter for free field geometry and in the following years *Bobber and Sabin* (1961) extended the analysis to cylindrical waves and finally for generalized geometries (*Bobber*, 1966).

With the advent of reciprocity the many limitations associated with hydrophone calibration were no longer present. As long as the devices were reciprocal, researchers could calibrate their hydrophones to sufficient accuracy without needing to trace those measurements. However, due to the complexity of deriving the reciprocity parameter in non-standard geometries as well as the difficulty in the setup, it was not universally used. Additionally, reciprocity calibration cannot be performed on digital hydrophones due to the need to measure both the transmitted current and received voltage. The most common method of calibration is still the reference method which involves comparison of unknown units to calibrated references. In this case the reference device is traced back to a reciprocal calibration from a previous measurement. The current hydrophone calibration standard IEC 60565-1:2020 includes both the reference method as well as reciprocity as valid calibration techniques (IEC 60565-1:2020).

Free field reference calibration, as described in part one of IEC 60565-1, is the most common technique for calibration, however it has many practical issues for general use. Free-field calibration requires a minimum of 1 wavelength of separation distance and the sensors must be sufficiently far away from any surface such that there is no interference due to reflections (IEC 60565-1:2020). This last requirement is typically the limiting factor on test environments. For a given test environment there is a lower frequency bound below which calibration cannot be accurate. Given the high speed of sound in water compared to air, performing reliable calibration below 10 kHz would require a tank with the smallest dimension of at least 2 m. Tanks of these sizes are expensive to build and maintain and are rare for most researchers and hydrophone manufacturers. Additionally, many current areas of ocean acoustic research involve frequencies less than 10 kHz such as seismic monitoring and ship noise which would require an even larger tanks.

For calibration below 2 kHz there have been many different systems constructed all based on hydrostatic pressure. First proposed by *Schloss and Strasberg* (1962) this system

sets the hydrophone in a vibrating chamber with a pressure sensor. The system allows for low frequency calibration by assuming that, for sufficiently large wavelength, the local variation in pressure throughout the tank is small. If this is the case the pressure in the entire chamber can be approximated to vary hydrostatically. This system is ideal for seismic hydrophone calibration as those signals are typically less than 10 Hz (*Dakin et al.*, 2014).

Variations of this system have been investigated to include the calibration while under a hydrostatic load. Traditional calibrations are performed in shallow water less than 10 m deep. However, hydrophone deployments typically are done in deeper water. Due to the nature of the piezoceramic inside the hydrophone, hydrostatic pressure has an effect on the calibration. This effect is more significant at low frequencies as was recognized by *Golenkov and Rachkov* (1980) was well as *Dakin et al.* (2014). Another technique based on Schloss' method was proposed by *Joubert et al.* (2015) where instead of a vibrating column of liquid the hydrophone is placed in a chamber with a step function pressure change. As the spectrum of a step function is broadband this change in pressure should allow for calibration for the entire system response.

The above methods rely on the local variation of pressure within the test environment to be negligible. This is the case for frequencies below 2 kHz but becomes impractical above 2 kHz. Techniques for mid-frequency calibration (1 kHz - 10 kHz) are still relatively unexplored. To perform calibration between 1 and 10 kHz, large tanks are needed to create the free field environment. A method described by *Johnson and Garrett* (1985) in a Naval Post Graduate School thesis confined the sound to a cylindrical waveguide. A compliant cylindrical waveguide has a reduced group speed, which effectively decreases the wavelength of the standing wave trapped in the guide for the same frequency in a free field. This allows for a smaller test setup. The thesis research attempted to perform a reciprocity calibration and calculated the reciprocity parameter for the tube by measurement of its quality factor (Q) and its resonance frequency. The experiment was done using a PVC tube, but this proved to be an issue as PVC has a negligible elastic range. The tube deformed and dissipated too much energy through expansion of the tube wall. Despite the plastic deformation, the results from the thesis were reproducible to +/- 0.8 dB. However, the hydrophone sensitivity had a systemic bias of 1.5 dB.

When calibrating hydrophones, special techniques are needed in order to calibrate across the whole spectrum of frequencies. For frequencies between 1 kHz and 10 kHz, Johnson proposed a system that was accessible to researchers without large costs. There is potential for improving the methods from Johnson by using copper piping rather than PVC to minimize the effect of energy loss from plastic deformation. Since copper has a defined elastic range it will not dissipate as much sound and minimize the issues with PVC.

To confirm that the copper piping is sufficiently rigid, the speed of sound of the pipe will be measured to characterize the sound field within the pipe If the system has low energy loss this will allow for a consistent calibration at low frequencies. Rather than focusing on reciprocity this research focuses on reference calibration which is simpler to perform and will be useful to the ocean technology industry.

CHAPTER 2

INTRODUCTION: THEORY OF SOUND IN PIPES

2.1 History of sound in pipes

In order to use the methods described by Johnson, an understanding on how sound travels in a pipe is critical. Sound transmission in a cylindrical waveguide has been a topic of study for over 150 years. The simplest case considers sound transmission with idealized pipe structure. *Rossing and Fletcher* (2004) solve this idealized case by starting with the acoustic wave equation in cylindrical coordinates

$$\nabla^2 p - \frac{1}{c}\frac{\partial^2 p}{\partial t^2} = 0, \tag{2.1}$$

where c is the speed of sound of the fluid and p is the acoustic pressure. The solution of the above partial differential equation (PDE) is given by the expression

$$p_{mn}(r,\theta,z,t) = p_0 P^{\cos}_{\sin}(n\theta) J_n\left(r\sqrt{k^2 - q_{nm}^2}\right) e^{i(q_{nm}z - \omega t)}, \tag{2.2}$$

where b is the pipe radius, ω is the angular frequency, p_0 is the initial pressure and P refers to the nth Legendre polynomial. The propagation wavenumber q_{nm} is defined so that the boundary condition for the idealized case ($\frac{\partial p}{\partial r} = 0$) is satisfied for a given n and m. From this formulation n and m are integers corresponding to modes that can exist in the pressure field. A key takeaway from this idealized case is the existence of the modes

and in particular the mode dependent wavenumber q_{nm}. These modes all have different wavelength for a single transmitting frequency. It can be shown that this wavelength is both a function of frequency and phase speed but depends also on the mode number. The wavenumber q_{nm} is calculated as

$$q_{nm}^2 = \left(\frac{\omega}{c}\right)^2 - \left(\frac{X_{nm}}{b}\right)^2, \tag{2.3}$$

where for rigid boundaries X_{nm} is the mth zero of $J_n'(x)$ and b is the inner pipe radius. Equation 2.3 implies a cutoff frequency ω_c the wavenumber will be purely imaginary. For a given mode (m,n) this cutoff only occurs when $\omega > \omega_c$, where

$$\omega_c = \frac{X_{nm}c}{b}. \tag{2.4}$$

Referring to equation 2.2, an imaginary wavenumber will cause that mode to decay exponentially in z rather than propagate in space. All the modes (including non-propagating ones) must exist to at $z = 0$ to satisfy the initial conditions. The plane wave $(0, 0)$ will always propagate but for higher modes there is a minimum frequency needed for propagation. This is not always the case for general boundary conditions.

For most applications involving in-air acoustics, the idealized boundary conditions are sufficient. The first attempts to add non-ideal effects to the wave propagation were done by *Stokes* (1845) and *von Helmholtz* (1863). These first treatments considered the effect of viscosity from the interaction between the fluid and the pipe wall. Later *Kirchhoff* (1868) added thermal effects to consider how heat transfer from the pipe wall into the fluid affected the propagation. There have been numerous studies since Kirchhoff's research investigating the sound transmission and energy loss with thermal and viscous effects. Examples include *Morse* (1939), *Daniels* (1950), *Benade* (1968) and *Keefe* (1984). As the main application in the previous studies was for air-filled pipes, losses due to an elastic boundary were not considered. When considering propagation in fluids with large bulk moduli, this assumption is no longer valid. (*Lin and Morgan*, 1956; *Gazis*, 1959; *Del Grosso*, 1964; *Del Grosso and McGill*, 1968; *Del Grosso*, 1968; *Del Grosso and McGill*, 1970; *Del Grosso*, 1971; *Zemanek Jr*, 1972; *Peterson*, 1974; *Fuller and Fahy*, 1982; *Sinha et al.*, 1992; *Plona et al.*, 1992; *Lafleur and Shields*, 1995; *Elvira-Segura*,

2000; *Wilson et al.*, 2003).

The first attempts to extend the analysis past air acoustics were done by *Lin and Morgan* (1956) and *Gazis* (1959). Both of these treatments did not solve the system with elastic boundaries analytically but used approximations to create expressions for the low-frequency dispersion of the system. The first true full analytically solution was given by *Del Grosso* (1968) in part 4 of his work on ultrasonic propagation. Del Grosso derives, using the elastic properties of material, the characteristic function as well as the mode shapes for a general pipe at all frequencies. Del Grosso later expanded on this work in 1968, 1970, and 1971 numerically calculating the dispersion for specific pipes and determining the pressure fields with input sources (*Del Grosso and McGill*, 1968, 1970; *Del Grosso*, 1971). Significantly Del Grosso limited his analysis to the axisymmetric waves (i.e. $m = 0$). A detailed discussion of this analysis is given in section 2.4. Other researchers extended and tested Del Grosso's work such as *Fuller and Fahy* (1982), *Sinha et al.* (1992); *Plona et al.* (1992) and *Lafleur and Shields* (1995). A treatment of the non-axisymmtric modes is given by *Zemanek Jr* (1972).

Modern work on this topic has focused on the non-linearities of the problem such as considering viscous fluids and viscoelastic pipe materials. The first to consider these scenarios were *Morgan and Kiely* (1954) for viscous fluids and *Klip et al.* (1967) for viscoelastic pipes. More work on the viscous fluids was done by *Chow and Apter* (1968), *Rubinow and Keller* (1971) and *Bansevičius and Kargaudas* (2005). Studying the effects of viscoelastic boundary conditions, work has been done by several researchers including *Rubinow and Keller* (1971), *Greenspon and Singer* (1995) and *Prek* (2007). Additionally *Rama Rao and Vandiver* (1999) looked into problems of this type with application to boreholes and *Kwun et al.* (1999) investigated the effects of welds on the dispersion.

2.2 Pressure field solution with rigid boundaries

Consider a straight fluid-filled pipe of radius b with rigid boundary conditions shown in figure 2.1. The pressure field inside the pipe is given by the wave equation for velocity potential Φ

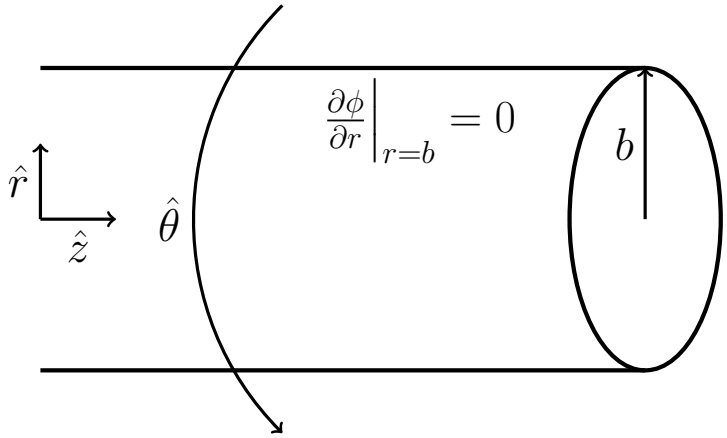

Figure 2.1: Diagram of a tube with rigid boundary conditions

$$\nabla^2 \Phi - \frac{1}{c^2}\frac{\partial^2 \Phi}{\partial t^2} \tag{2.5}$$

where c is the phase speed of sound of the fluid. The particle velocity $\vec{u}$ and pressure p can be found from the potential as

$$\vec{u} = \boldsymbol{\nabla} \Phi \tag{2.6}$$

$$p = -\rho_L \frac{\partial}{\partial t}\Phi, \tag{2.7}$$

where ρ_L is the density of the fluid. In cylindrical coordinates the potential is a function of r, θ, z and t. Equation 2.5 is separable into two expressions $\phi(r, \theta, z)$ and $T(t)$ such that $\Phi = \phi T$. Using $-k^2$ as the separation constant the equations become

$$\nabla^2 \phi + k^2 \phi = 0 \tag{2.8}$$

$$\frac{\mathrm{d}^2 T}{\mathrm{d}t^2} = -k^2 c^2 T. \tag{2.9}$$

Equation 2.8 is the Helmholtz equation and equation 2.9 is the equation of simple harmonic motion with frequency $\omega = kc$. The latter equation has solutions

$$T(t) = e^{\pm i\omega t}. \tag{2.10}$$

Looking at the Helmholtz equation, the Laplacian can be written in cylindrical polar coordinates which gives the expanded equation

$$\frac{1}{r}\frac{\partial}{\partial r}\left(r\frac{\partial \phi}{\partial r}\right)+\frac{1}{r^2}\frac{\partial^2 \phi}{\partial \theta^2}+\frac{\partial^2 \phi}{\partial z^2}+k^2\phi=0. \tag{2.11}$$

Equation 2.11 can be further separated into three ordinary differential equations (ODE) $\phi(r,\theta,z)=R(r)\Theta(\theta)Z(z)$ by introducing the separation constants $-n^2$ and $-q^2$. The three equations become

$$\frac{\mathrm{d}^2 R}{\mathrm{d}r^2}+\frac{1}{r}\frac{\mathrm{d}R}{\mathrm{d}r}+R\left[\left(k^2-q^2\right)-\frac{n^2}{r^2}\right]=0 \tag{2.12}$$

$$\frac{\mathrm{d}^2 \Theta}{\mathrm{d}\theta^2}=-n^2\Theta \tag{2.13}$$

$$\frac{\mathrm{d}^2 Z}{\mathrm{d}z^2}=-q^2 Z. \tag{2.14}$$

The solutions to equations 2.13 and 2.14 are as given simple harmonic motion in θ and z respectively

$$\Theta = A\cos(n\theta)+B\sin(n\theta) \tag{2.15}$$

$$Z = Ce^{iqz}+De^{-iqz}, \tag{2.16}$$

where A, B, C and D are arbitrary constants determined from conditions on the original PDE. Equation 2.12 can also be solved by inspection as this is Bessel's equation which has two linearly independent solutions $J_\nu(x)$ and $Y_\nu(x)$. This gives the expression for R as

$$R=EJ_n\left(r\sqrt{k^2-q^2}\right)+FY_n\left(r\sqrt{k^2-q^2}\right), \tag{2.17}$$

where again E and F are arbitrary constants. As the domain of the R equation is $r=[0,b]$ this requires that $F=0$ as $Y_n(x)$ is singular at $x=0$. Additionally, applying the radiation condition requires $D=0$. This gives the full expression of the time-independent potential for a mode of order (n,m)

$$\phi_{nm}=\Theta(\theta)J_n\left(r\sqrt{k^2-q_{nm}^2}\right)e^{iq_{nm}z}, \tag{2.18}$$

where m is determined by the boundary conditions. Now limiting the discussion to modes with axial symmetry per *Del Grosso* (1964, 1968) the θ dependent part of the equation is removed by setting $n = 0$. This gives the full time-dependent potential as

$$\Phi_{0m} = \Phi_{0m} J_0 \left(\frac{r X_{0m}}{b} \right) e^{i(q_{0m} z - \omega t)}, \tag{2.19}$$

where X_{0m} is a characteristic value

$$X_{0m} = b\sqrt{k^2 - q_{0m}^2}, \tag{2.20}$$

such that the r dependent portion of the potential becomes $J_0 \left(r \frac{X_{0m}}{b} \right)$.

The value q_{0m} can be thought of as the wavenumber for the mth mode propagating in the z direction. This wave propagates with a phase speed of $c_{0m} = \omega / q_{0m}$. Another interpretation is that the modes all propagate at the phase speed of the liquid but at different starting angles. The interference pattern is then what governs the apparent change in propagation speed. Recall that in the argument for the Bessel function in equation 2.18 the expression looks similar to a Pythagorean triple. Defining $k_r = \sqrt{k^2 - q_{0m}^2}$, this value is now the radial "wavenumber" such that $k^2 = k_r^2 + q_{0m}^2$. The angle that the k vector forms with z-axis $\gamma = \arccos\big(q_{0m}/k\big)$ is the angle of propagation of the plane wave for each mode m. Unlike in the z direction with q_{0m}, the r dependence is not sinusoidal however the assymtopic expansion of Bessel function

$$J_0(x) \sim \sqrt{\frac{2}{\pi x}} \cos\big(x - \pi/4\big), \tag{2.21}$$

does converge to a sinusoid for large radii.

The full pressure field expression can be found using the relation given in equation 2.7.

$$p = -\rho_L \frac{\partial}{\partial t} \Phi = i \rho_L \omega E_{0m} J_0 \left(r \frac{X_{0m}}{b} \right) e^{i(q_{0m} z - \omega t)}. \tag{2.22}$$

Note that the pressure expression is multiplied by the imaginary constant i ($i^2 = -1$) and is a complex value. This is just to ease calculations, the true pressure is the real component of expression 2.22.

The question then becomes, what are the values of q_{0m} to determine the dispersion of the modes. This is determined from the boundary conditions. Up until this point, the fact that the pipe walls are rigid has not been used. For rigid boundaries

$$\frac{\partial}{\partial r}\phi_{0m}\bigg|_{r=b} = 0. \tag{2.23}$$

Taking the r partial derivative of the potential yields

$$\frac{\partial}{\partial r}\phi = E_{0m}\frac{X_{0m}}{a}J_0'\left(r\frac{X_{0m}}{b}\right)e^{iq_{0m}z}, \tag{2.24}$$

using the relation that $J_0'(x) = -J_1(x)$ and applying the condition

$$\frac{\partial}{\partial r}\phi_{0m}\bigg|_{r=b} = E_{0m}\frac{-X_{0m}}{b}J_1\left(X_{0m}\right)e^{iq_{0m}z} = 0, \tag{2.25}$$

which is only non-trivially zero if $J_1\left(X_{0m}\right) = 0$. This gives a meaning to the value m as X_{0m} is defined as the m^{th} zero of $J_1\left(x\right)$.

2.3 Phase and group speed

When propagating in free space, waves travel at a constant speed which is intrinsic to the material regardless of frequency. This is not the case when the sound is confined within a waveguide. While in a waveguide there are two quantities that are needed to describe the propagation speed: phase speed and group speed. The phase speed

$$c_p = \frac{\omega}{k}, \tag{2.26}$$

where ω is the angular frequency in rad/s and k is the wavenumber in the propagation direction. This represents the speed at which the phase of the wave propagates. The quantity does not describe the speed at which the wave's energy (and thus the wave packet) travels through space. This is known as the group speed defined as

$$c_g = \frac{\partial\omega}{\partial k}. \tag{2.27}$$

Note that in the free field both c_p an c_g are the same and referred to as c or the intrinsic sound speed.

In the cylindrical waveguide, the wavenumber in the propagation direction is q_{0m} and thus the phase speed is found with equation 2.26 and by substituting in equation 2.20

$$c_{p_{0m}} = \frac{\omega}{\sqrt{k^2 - \left(\frac{X_{0m}}{b}\right)^2}}. \tag{2.28}$$

Recalling that the intrinsic speed c is given as ω/k the phase speed in the cylindrical waveguide is further simplified into

$$c_{p_{0m}} = \frac{c}{\sqrt{1 - \left(\frac{X_{0m}}{kb}\right)^2}}. \tag{2.29}$$

Expression 2.29 implies the existence of imaginary phase speeds when $X_{0m} > kb$ and no propagation occurs. The group velocity is derived by rearranging equation 2.20 to find the frequency as a function of wavenumber

$$\omega(q_{0m}) = \sqrt{q_{0m}^2 c^2 + \left(\frac{X_{0m}}{b}\right)^2 c^2}. \tag{2.30}$$

Applying the definition of the group velocity from equation 2.27 gives

$$c_{g_{0m}} = \frac{\partial \omega}{\partial q_{0m}} = \frac{q_{0m} c^2}{\sqrt{q_{0m}^2 c^2 + \left(\frac{X_{0m}}{b}\right)^2 c^2}}. \tag{2.31}$$

Recalling that the denominator is simply the frequency ω and substituting in equation 2.30 and the phase speed expression equation 2.31 is simplified to

$$c_{g_{0m}} = c\sqrt{1 - \left(\frac{X_{0m}}{kb}\right)^2}, \tag{2.32}$$

where both $c_{p_{0m}}$ and $c_{g_{0m}}$ are related through

$$c^2 = c_{p_{0m}} c_{g_{0m}}. \tag{2.33}$$

The group speeds also exhibit the same frequency cutoff for imaginary wavenumber as the phase speeds. While performing calibrations, to determine the first arrival of the wave packet, the quantity of interest is the group speed and needs to be determined for the elastic waveguide to perform the measurements.

2.4 Effect of the elastic boundary conditions

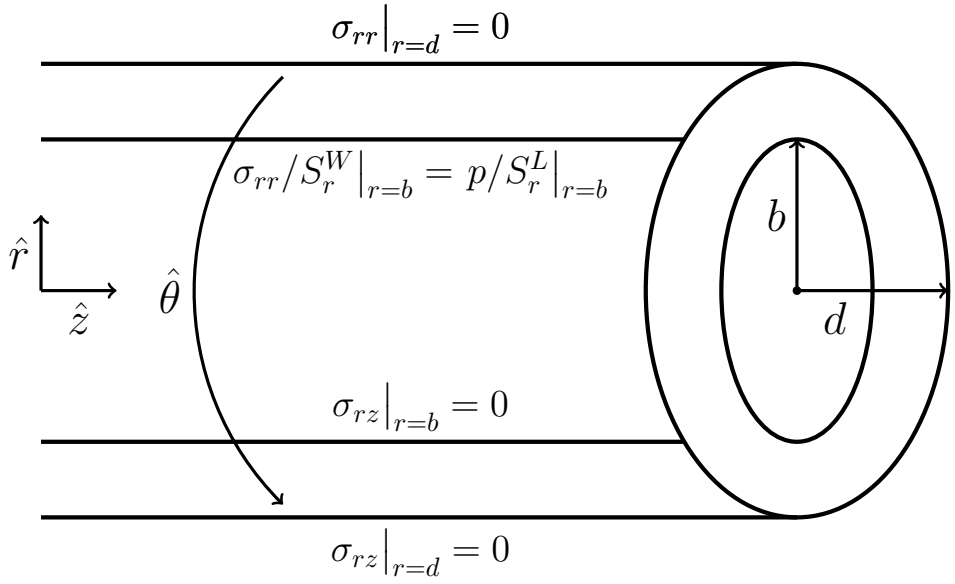

Figure 2.2: Diagram of a tube with elastic boundary conditions

From the results in section 2.2, the velocity potential inside the liquid cylinder is given by equation 2.19. When considering elastic boundaries, the corresponding potential fields within the pipe wall also need to be determined. A diagram of the elastic pipe is shown in figure 2.2. Using the method provided by *Del Grosso* (1968), a displacement vector $\vec{S}$ is defined in terms of a scalar displacement potential Ξ and a vector displacement potential $\vec{\Psi}$ as

$$\vec{S} = \boldsymbol{\nabla}\Xi + \boldsymbol{\nabla} \times \vec{\Psi}, \tag{2.34}$$

where both Ξ and $\vec{\Psi}$ are solutions to the wave equations

$$\nabla^2 \Xi = \frac{1}{c}\frac{\partial^2 \Xi}{\partial t^2} \tag{2.35}$$

$$\nabla^2 \vec{\Psi} = \frac{1}{c}\frac{\partial^2 \vec{\Psi}}{\partial t^2}. \tag{2.36}$$

As the material in the wall is elastic the equations of motion necessarily obey Hooke's law such that

$$\rho_W \frac{\partial^2 \vec{S}}{\partial t^2} = (L + 2\mu)\boldsymbol{\nabla}\left(\boldsymbol{\nabla} \cdot \vec{S}\right) - 2\mu\boldsymbol{\nabla} \times \left(\frac{1}{2}\boldsymbol{\nabla} \times \vec{S}\right) \tag{2.37}$$

where L and μ are Lamé's constants and ρ_W is the density of the wall material.

In cylindrical coordinates the components of equation 2.34 are

$$\boldsymbol{\nabla}\Xi = \frac{\partial \Xi}{\partial r}\hat{\boldsymbol{r}} + \frac{1}{r}\frac{\partial \Xi}{\partial \theta}\hat{\boldsymbol{\theta}} + \frac{\partial \Xi}{\partial z}\hat{\boldsymbol{z}} \tag{2.38}$$

and

$$\begin{aligned} \boldsymbol{\nabla} \times \vec{\Psi} = &\left[\frac{1}{r}\frac{\partial}{\partial \theta}\Psi_z - \frac{\partial}{\partial z}\Xi_\theta\right]\hat{\boldsymbol{r}} \\ &+ \left[\frac{\partial}{\partial z}\Psi_r - \frac{\partial}{\partial r}\Xi_z\right]\hat{\boldsymbol{\theta}} \\ &+ \frac{1}{r}\left[\frac{\partial}{\partial r}(\Psi_\theta) - \frac{\partial}{\partial \theta}\Xi_r\right]\hat{\boldsymbol{z}}. \end{aligned} \tag{2.39}$$

Combing equations 2.38 and 2.39 the vector displacement $\vec{S} = S_r\hat{\boldsymbol{r}} + S_\theta\hat{\boldsymbol{\theta}} + S_z\hat{\boldsymbol{z}}$ can be represented as

$$S_r = \frac{\partial \Xi}{\partial r} + \frac{1}{r}\frac{\partial \Psi_z}{\partial \theta} - \frac{\partial \Psi_\theta}{\partial z} \tag{2.40}$$

$$S_\theta = \frac{1}{r}\frac{\partial \Xi}{\partial \theta} + \frac{\partial \Psi_r}{\partial z} - \frac{\partial \Psi_z}{\partial r} \tag{2.41}$$

$$S_z = \frac{\partial \Xi}{\partial z} + \frac{1}{r}\left[\frac{\partial (r\Psi_\theta)}{\partial r} - \frac{\partial \Psi_r}{\partial \theta}\right]. \tag{2.42}$$

Assuming axial symmetry, ($S_\theta = 0$ and $\frac{\partial}{\partial \theta} = 0$) the components of displacement are reduced to

$$S_r = \frac{\partial \Xi}{\partial r} - \frac{\partial \Psi_\theta}{\partial z} \tag{2.43}$$

$$S_z = \frac{\partial \Xi}{\partial z} + \frac{1}{r}\frac{\partial (r\Psi_\theta)}{\partial r}. \tag{2.44}$$

As there is only one component of $\vec{\Psi}$ remaining, for the remainder of the analysis $\Psi_\theta = \Psi$. The two wave equations 2.35 and 2.36 now can be written as the "wave" equations

$$\nabla^2 \Xi - \frac{1}{c_c^2}\frac{\partial^2 \Xi}{\partial t^2} = 0 \tag{2.45}$$

$$\nabla^2 \Psi - \frac{\Psi}{r^2} - \frac{1}{c_s^2}\frac{\partial^2 \Psi}{\partial t^2} = 0, \tag{2.46}$$

where "wave" refers to the extra term of $\frac{\Psi}{r^2}$ and c_c and c_s are the compression and shear speed in the wall material respectively. The extra term in the ψ equation comes from the definition of the vector Laplacian in cylindrical coordinates

$$\begin{aligned} \nabla^2 \vec{\Psi} = &\left(\nabla^2 \Psi_r - \frac{\Psi_r}{r^2} - \frac{2}{r^2}\frac{\partial \Psi_r}{\partial \theta} \right) \hat{\boldsymbol{r}} \\ &+ \left(\nabla^2 \Psi_\theta - \frac{\Psi_\theta}{r^2} + \frac{\partial \Psi_\theta}{\partial \theta} \right) \hat{\theta} \\ &+ \nabla^2 \Psi_z \hat{\boldsymbol{z}}. \end{aligned} \tag{2.47}$$

As with the rigid boundary discussion in section 2.2 these equations are solved through separation of variables by first removing the time dependence $e^{i\omega t}$ and the axial dependence $e^{iq_{0m}z}$ leaving the two r equations

$$\frac{\mathrm{d}^2 \Xi}{\mathrm{d}r^2} + \frac{1}{r}\frac{\mathrm{d}\Xi}{\mathrm{d}r} + \left[(k_c^2 - q_{0m}^2) - \frac{0^2}{r^2} \right] \Xi = 0 \tag{2.48}$$

$$\frac{\mathrm{d}^2 \Psi}{\mathrm{d}r^2} + \frac{1}{r}\frac{\mathrm{d}\Psi}{\mathrm{d}r} + \left[(k_s^2 - q_{0m}^2) - \frac{1^2}{r^2} \right] \Psi = 0. \tag{2.49}$$

These two equations have Bessel function solutions $J_n(x)$ and $Y_n(x)$ of the form

$$\Xi = \left[AJ_0(P_m r) + BY_0(P_m r)\right] e^{i(q_{0m}z-\omega t)} \qquad b < r < d \tag{2.50}$$

$$\Psi = \left[CJ_1(T_m r) + DY_1(T_m r)\right] e^{i(q_{0m}z-\omega t)}, \tag{2.51}$$

where $P_m = \sqrt{k_c^2 - q_{0m}^2}$ and $T_m = \sqrt{k_s^2 - q_{0m}^2}$. Once again $A,\ B,\ C,\ D$ are arbitrary constants that are determined from the boundary conditions. In the above expressions $k_c = \omega/c_c$ and $k_s = \omega/c_s$ Note that unlike the the expression for the field in the liquid the Bessel function of the second kind remains in equations 2.50 and 2.51. This is because neither function is singular on the boundary $r = b$ and $r = d$. From section 2.2, the velocity potential for the guided waves inside the liquid ($r < b$) is given by equation 2.19. For the case of the elastic the analysis is done with displacement potential, the displacement potential in the liquid is given by

$$\Xi = \Xi_0 J_0\left(\frac{rX_{0m}}{b}\right) e^{i(q_{0m}z-\omega t)} \qquad r < b, \tag{2.52}$$

where Ξ is a displacement potential in the liquid. Note that the displacement in the liquid is given by $S_z^L = \frac{\partial}{\partial z}\Xi$ and $S_r^L = \frac{\partial}{\partial r}\Xi$. The pressure and particle velocity in the radial direction is given as

$$p = -\rho_L \ddot{\Xi} \tag{2.53}$$

$$U_r^L = \frac{\partial}{\partial r}\dot{\Xi}. \tag{2.54}$$

Using the relation between the potential and the displacement, the displacement in the liquid is

$$S_z^L(r,z,t) = i\Xi_0 q_{0m} J_0\left(r\frac{X_{0m}}{b}\right) e^{i(q_{0m}-\omega t)} \tag{2.55}$$

$$S_r^L(r,z,t) = \frac{-\Xi_0 X_{0m}}{b} J_1\left(r\frac{X_{0m}}{b}\right) e^{i(q_{0m}-\omega t)}, \tag{2.56}$$

and in the pipes

$$S_z^W = \left[iq_{0m} \left(AJ_0 \left(rP_m \right) + BY_0 \left(rP_m \right) \right) + T_m \left(CJ_0 \left(rT_m \right) + DY_0 \left(rT_m \right) \right) \right] e^{i(q_{0m} - \omega t)} \tag{2.57}$$

$$S_r^W = \left[-P_m \left(AJ_1 \left(rP_m \right) + BY_1 \left(rP_m \right) \right) - iq_{0m} \left(CJ_1 \left(rT_m \right) + DY_1 \left(rT_m \right) \right) \right] e^{i(q_{0m} - \omega t)}. \tag{2.58}$$

In the case of the rigid boundary, there was only one boundary condition that needed to be applied to the system $\frac{\partial}{\partial r}\Phi\Big|_{r=b} = 0$. With elastic boundaries with finite wall thickness there are four conditions that must be satisfied

$$\sigma_{rr}\Big|_{r=d} = 0 \tag{2.59}$$

$$\sigma_{rz}\Big|_{r=d} = 0 \tag{2.60}$$

$$\sigma_{rz}\Big|_{r=b} = 0 \tag{2.61}$$

$$\frac{-\sigma_{rr}}{S_r^W}\Big|_{r=b} = \frac{p}{S_r^L}\Big|_{r=b}, \tag{2.62}$$

where σ_{rr} and σ_{rz} are components of the full stress tensor. The expressions for the stress components are

$$\sigma_{rr} = 2\mu \frac{\partial S_r^W}{\partial r} + L \left(\frac{\partial S_r^W}{\partial r} + \frac{S_r^W}{r} + \frac{\partial S_z^W}{\partial z} \right) \tag{2.63}$$

$$\sigma_{rz} = \mu \left(\frac{\partial S_r^W}{\partial z} + \frac{\partial S_z^W}{\partial r} \right), \tag{2.64}$$

where the shear modulus $\mu = \rho_w c_s^2$ and L is the other Lamé constant $L = 2\rho_W c_s^2 \left(\frac{\nu}{1-2\nu} \right)$ with ν being Poisson's ratio.

The expressions for the four boundary conditions in terms of the displacements in equations 2.55- 2.58 is given by *Del Grosso* (1968) and *Lafleur and Shields* (1995). The first condition requires that the tangential stress on the liquid-solid boundary is zero

$$\sigma_{rr}\Big|_{r=d} = 0. \tag{2.65}$$

Applying this condition by evaluating equation 2.63 in terms of the displacements gives

$$A\left(E_m J_0\left(dP_m\right)+\frac{P_m}{d}J_1\left(dP_m\right)\right)+B\left(E_m Y_0\left(dP_m\right)+\frac{P_m}{d}Y_1\left(dP_m\right)\right)+$$
$$C\left(-iq_{0m}T_m J_0\left(dT_m\right)+i\frac{q_{0m}}{d}J_1\left(dT_m\right)\right)+D\left(-iq_{0m}T_m Y_0\left(dT_m\right)+i\frac{q_{0m}}{d}Y_1\left(dT_m\right)\right)=0. \tag{2.66}$$

Similarly for the two conditions on the shear stress

$$\sigma_{rr}\Big|_{r=d}=0, \qquad \sigma_{rr}\Big|_{r=b}=0, \tag{2.67}$$

gives the two following expressions

$$\begin{aligned} &A\left[iq_{0m}P_m J_1\left(dP_m\right)\right]+B\left[iq_{0m}P_m Y_1\left(dP_m\right)\right]+\\ &C\left[-E_m J_1\left(dT_m\right)\right]+D\left[-E_m Y_1\left(dT_m\right)\right]=0, \end{aligned} \tag{2.68}$$

and

$$\begin{aligned} &A\left[iq_{0m}P_m J_1\left(bP_m\right)\right]+B\left[iq_{0m}P_m Y_1\left(bP_m\right)\right]+\\ &C\left[-E_m J_1\left(bT_m\right)\right]+D\left[-E_m Y_1\left(bT_m\right)\right]=0. \end{aligned} \tag{2.69}$$

Finally the last condition requires that the tangential stress and the displacement must be continuous at the boundary $r=b$

$$\frac{-\sigma_{rr}}{S_r}\Big|_{r=b}=\frac{p}{S_r^L}\Big|_{r=b}, \tag{2.70}$$

which gives the final expression

$$\begin{aligned} &A\left(E_m J_0\left(bP_m\right)+\frac{1+Q_m b}{b}P_m J_1\left(bP_m\right)\right)+\\ &B\left(E_m Y_0\left(bP_m\right)+\frac{1+Q_m b}{b}Y_1\left(bP_m\right)\right)+\\ &C\left(-iq_{0m}T_m J_0\left(bT_m\right)+\frac{iq_{0m}}{b}(1+Q_m b)J_1\left(bT_m\right)\right)+\\ &D\left(-iq_{0m}T_m Y_0\left(bT_m\right)+\frac{iq_{0m}}{b}(1+Q_m b)Y_1\left(bT_m\right)\right)=0, \end{aligned} \tag{2.71}$$

where in equations 2.66 to 2.71

$$E_m - q_{0m}^2 - k_s^2/2 \tag{2.72}$$

$$Q_m = \frac{\rho_L \omega^2 b J_0\left(X_{0m}\right)}{2\rho_W c_s^2 X_{0m} J_1\left(X_{0m}\right)} \tag{2.73}$$

Non-zero values of the constants A, B, C, and D are found when the determinant of their coefficients in equations 2.66 to 2.71 vanish. This occurs at specific pairs of (ω_c, q_{0m}). From the boundary conditions a characteristic equation relating q_{0m} to ω is found as

$$\begin{aligned}
1+ &\left[L_{11}(P_m)L_{00}(T_m)\right]\left(\frac{\pi^2 q_{0m}^2 b d P_m^2 T_m^2}{8E_m^2}\right) + \left[L_{11}(T_m)L_{00}(P_m)\right]\left(\frac{\pi^2 b d E_m^2}{8q_{0m}^2}\right) + \\
&\left[L_{10}(P_m)L_{01}(T_m) + L_{01}(P_m)L_{10}(T_m)\right]\left(\frac{\pi^2 b d P_m T_m}{8}\right) + \\
&\left[bL_{11}(P_m)L_{10}(T_m) + d(1+Q_m b)L_{11}(P_m)L_{01}(T_m)\right]\left(\frac{\pi^2 P_m^2 T_m}{8E_m} - \frac{\pi^2 P_m^2 q_{0m}^2 T_m}{8E_m^2}\right) + \\
&\left[bL_{11}(T_m)L_{10}(P_m) + d(1+Q_m b)L_{11}(T_m)L_{01}(P_m)\right]\left(\frac{\pi^2 P_m E_m}{8q_{0m}^2} - \frac{\pi^2 P_m}{8}\right) + \\
&\left[(1+Q_m b)L_{11}(T_m)L_{11}(P_m)\right]\left(\frac{\pi^2 P_m^2}{8q_{0m}^2} + \frac{\pi^2 P_m^2 q_{0m^2}}{8E_m^2} - \frac{\pi^2 P_m^2}{4E_m}\right) = 0,
\end{aligned} \tag{2.74}$$

where $L_{mn}(y) = J_m\left(dy\right) Y_n\left(by\right) - J_n\left(by\right) Y_m\left(dy\right)$. In general for any given ω there are multiple solutions of q_{0m}. This suggests there are distinct modes that propagate in the z axis with speed found by via the expression $c_{0m} = \omega/q_{0m}$.

Equation 2.74 cannot be solved analytically but can be solved numerically for a given liquid, wall material and wall geometry. *Lafleur and Shields* (1995) gives a method to find the q_{0m} zeros by dividing the domain and range of interest into bins. First chose a frequency point and then search for zeros of the characteristic equation within the designated bin in q-space. The zeros are found by taking the real value of the characteristic then performing the secant method to search for zeros. As the q-bins are sufficiently small there will only be one zero in the range to converge to.

The parameters for the pipe used in these calibration experiments were put into a script

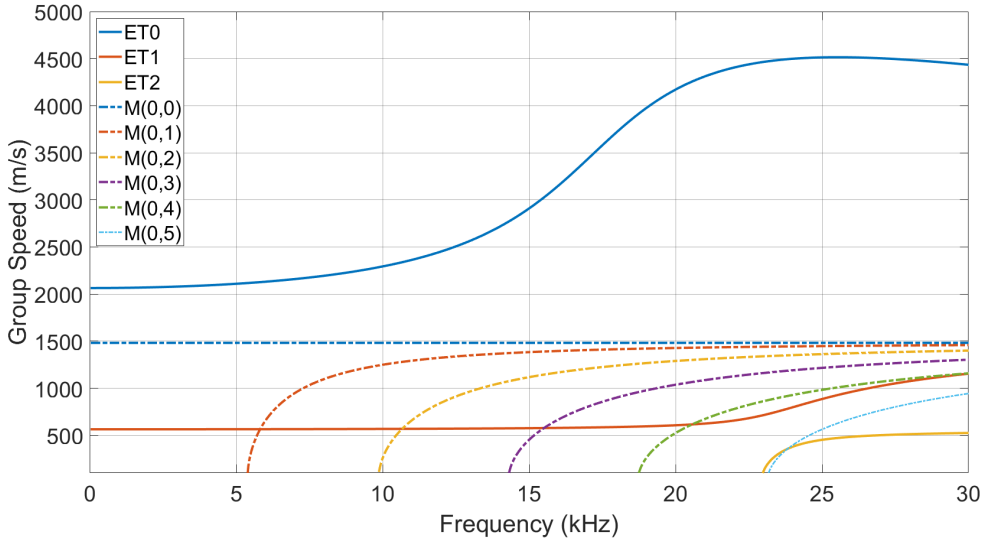

Figure 2.3: Modal group speed dispersion for a tube with rigid boundaries (M) and elastic boundaries (ET). Tube radius inner radius is 2.6 cm with wall thickness 1 mm

to find the dispersion of the modes. These parameters are from *Haynes* (2014) and are summarized in table 2.1. The plot of the modes is show in figure 2.3.

Table 2.1: Experimental parameters of the pipe used in the calibration

d (mm)	b (mm)	c_L (m/s)	c_c (m/s)	c_s (m/s)	ρ_L (kg/m^3)	$\rho_W (kg/m^3)$
169	168	1482	5010	2270	1000	8960

Figure 2.3 shows that the two lowest modes ($ET0$ and $ET1$ in Del Grosso's notation (*Del Grosso*, 1968)) are always propagating regardless of frequency and have no cutoff. The higher modes all have a cutoff frequency where their phase speed asymptotes to infinity. As well, unlike the case with the rigid pipe in section 2.2 one of the propagating modes (ET1) is both below the group speed of the liquid (in this case fresh water at 1482 m/s) and varies with frequency.

This result forms the basis for calibration as first proposed by *Johnson and Garrett* (1985). Since the group speed has decreased, calibration can be done at lower frequencies using the same tank dimensions.

2.5 Modal Amplitudes

It is also useful to consider the amplitude of the modes that are propagating. Once again using the methods from *Del Grosso* (1965), consider the velocity potential expansion for the symmetric modes given as

$$\phi(r,z) = \sum_{m=0} \phi_{0m} J_0\left(r\frac{X_{0m}}{b}\right) e^{iq_{0m}z}, \tag{2.75}$$

where ϕ_{0m} is the amplitude of the mth mode. To determine the values of ϕ_{0m} the condition that the initial field at $z = 0$ is some function of r determined by source geometry. Assuming the source can be approximated as a piston source of radius a the initial condition is

$$\phi_{0m}(r, z=0) = \begin{cases} \varphi_0, & r \le a \\ 0, & r > a \end{cases}, \tag{2.76}$$

where φ_0 is the initial field magnitude. Equations 2.75 and 2.76 are multiplied by $rJ_0\left(r\frac{X_{0l}}{b}\right)$ where l is an integer. Integrating across the inner radius gives

$$\int_0^b \varphi_0 J_0\left(r\frac{X_{0l}}{b}\right) r\,\mathrm{d}r = \int_0^b \sum_{m=0} \phi_{0m} J_0\left(r\frac{X_{0m}}{b}\right) J_0\left(r\frac{X_{0l}}{b}\right) r\,\mathrm{d}r\,, \tag{2.77}$$

where the left side of equation 2.77 can be evaluated as

$$\int_0^b \varphi_0 J_0\left(r\frac{X_{0l}}{b}\right) r\,\mathrm{d}r = \phi_0 \frac{ab}{X_{0l}} J_1\left(X_{0l}\frac{a}{b}\right). \tag{2.78}$$

For the right side, at $m = l$ a closed-form expression exists for all values of X_{0m}

$$\int_0^b \phi_{0m} J_0^2\left(r\frac{X_{0m}}{b}\right) r\,\mathrm{d}r = \phi_{0m}\frac{b^2}{2}\left[J_0^2\left(X_{0m}\right) + J_1^2\left(rX_{0m}\right)\right]. \tag{2.79}$$

This shows that a closed-form expressed for all modal amplitudes exists provided that the orthogonality relation

$$\int_0^b J_0\left(r\frac{X_{0m}}{b}\right) J_0\left(r\frac{X_{0l}}{b}\right) r\,\mathrm{d}r = 0, \qquad m \neq l, \tag{2.80}$$

holds for all possible values of X_{0m} and X_{0l}. Expression 2.80 is true for the characteristic values for a rigid pipe but is not true generally for the elastic waveguide. To calculate values of ϕ_{0m} a system of integrals can be constructed for all modes in the expansion. Defining $R_{nm} = J_n\left(r\frac{X_{0m}}{b}\right)$ the system of integrals is

$$\begin{aligned} l=0: \qquad \frac{ab}{X_{00}}J_1\left(X_{00}\frac{a}{b}\right) &= \int_0^b \phi_{00}R_{00}^2 r\,\mathrm{d}r + \int_0^b \phi_{01}R_{00}R_{01}r\,\mathrm{d}r \\ &\quad + \int_0^b \phi_{02}R_{00}R_{02}r\,\mathrm{d}r + \int_0^b \phi_{03}R_{00}R_{03}r\,\mathrm{d}r\ldots \end{aligned} \tag{2.81}$$

$$\begin{aligned} l=1: \qquad \frac{ab}{X_{01}}J_1\left(X_{01}\frac{a}{b}\right) &= \int_0^b \phi_{00}R_{01}R_{00}r\,\mathrm{d}r + \int_0^b \phi_{01}R_{01}^2 r\,\mathrm{d}r \\ &\quad + \int_0^b \phi_{02}R_{01}R_{02}r\,\mathrm{d}r + \int_0^b \phi_{03}R_{01}R_{03}r\,\mathrm{d}r\ldots \end{aligned} \tag{2.82}$$

$$\begin{aligned} l=2: \qquad \frac{ab}{X_{02}}J_1\left(X_{02}\frac{a}{b}\right) &= \int_0^b \phi_{00}R_{02}R_{00}r\,\mathrm{d}r + \int_0^b \phi_{01}R_{02}R_{01}r\,\mathrm{d}r \\ &\quad + \int_0^b \phi_{02}R_{02}^2 r\,\mathrm{d}r + \int_0^b \phi_{03}R_{02}R_{03}r\,\mathrm{d}r\ldots + \text{etc}\ldots \end{aligned} \tag{2.83}$$

Provided the the characteristic values are known for the given boundary conditions the system can be solved for the individual model amplitudes.

2.6 Effect due to the pipe curvature

The derivations in sections 2.2 and 2.4 assume that the pipe is straight. While simple to analyze, the investigated calibration system uses curved pipes to optimize space. To understand how the curvature affects the propagation, the rigid boundary analysis is done similar to section 2.2 for a curved section. This scenario is shown in figure 2.4. To simplify computation the analysis is done in 2-dimensions.

The natural coordinate system for this problem is cylindrical polar with the propagation direction being in $\hat{\theta}$. The Helmholtz equations is then

$$\frac{\partial^2\phi}{\partial r^2} + \frac{1}{r}\frac{\partial\phi}{\partial r} + \frac{1}{r^2}\frac{\partial^2\phi}{\partial\theta^2} + k^2\phi = 0 \tag{2.84}$$

where as before ϕ is a time-independent potential. Separating the equation by requiring

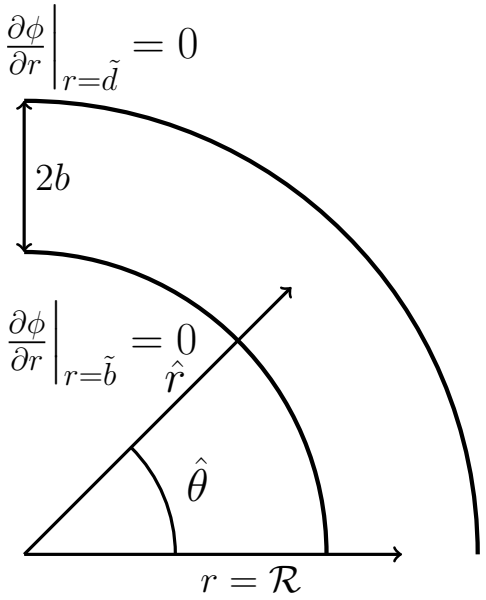

Figure 2.4: Diagram of a curved pipe with rigid boundary conditions

$\phi = R(r)\Theta(\theta)$ with the constant $\tilde{q}^2$ gives the equations

$$\frac{\mathrm{d}^2 R}{\mathrm{d}r^2} + \frac{1}{r}\frac{\mathrm{d}R}{\mathrm{d}r} + R\left[k^2 - \frac{\tilde{q}^2}{r^2}\right] = 0 \tag{2.85}$$

$$\frac{\mathrm{d}^2 \Theta}{\mathrm{d}\theta^2} = -\tilde{q}^2\Theta. \tag{2.86}$$

The solutions are found by inspection as

$$R = AJ_{\tilde{q}}(kr) + BY_{\tilde{q}}(kr) \tag{2.87}$$

$$\Theta = e^{\pm i\tilde{q}\theta}. \tag{2.88}$$

The separated solutions in equation 2.87 and 2.88 are different than the solutions from the rigid pipe. Unlike the previous development, this separation constant has units of 1/rad. Like before, the constant $\tilde{q}$ is the wavenumber in the propagation direction but it is an angular quantity. The previous relations for phase and group speed still hold but become

angular velocities with units of rad/s

$$\tilde{c}_p = \frac{\omega}{\tilde{q}} \tag{2.89}$$

$$\tilde{c}_g = \frac{\mathrm{d}\omega}{\mathrm{d}\tilde{q}}. \tag{2.90}$$

Another consideration is that both the Bessel functions of the first and second kind remain in equation 2.87 as $r = 0$ is not part of the domain. Additionally, the Bessel function order is not confined to be an integer but can be any positive real number.

Applying the boundary condition $R'(\tilde{b}) = 0$ to the R equation gives the expression

$$R(r) = A\left[J_{\tilde{q}(kr)} - \frac{J'_{\tilde{q}}(k\tilde{b})}{Y'_{\tilde{q}}(k\tilde{b})}Y_{\tilde{q}}(kr)\right]. \tag{2.91}$$

Applying the second condition $R'(\tilde{d}) = 0$ gives the characteristic equation

$$J'_{\tilde{q}}(k\tilde{b})Y'_{\tilde{q}}(k\tilde{d}) - Y'_{\tilde{q}}(k\tilde{b})J'_{\tilde{q}}(k\tilde{d}) = 0. \tag{2.92}$$

Equation 2.92 is known as the Bessel cross product. The valid values of $\tilde{q}$ (and thus the modes) for a given frequency is governed by the zeros of this equation. Using the series approximations for the Bessel functions, *Cochran* (1964) gives a power series solution for the mth zero of the equation as

$$x = \alpha + \frac{p}{\alpha}\ldots, \tag{2.93}$$

where

$$x = k\tilde{b} \tag{2.94}$$

$$\lambda = \tilde{d}/\tilde{b} \tag{2.95}$$

$$\alpha = \frac{(m-1)\pi}{\lambda - 1} \tag{2.96}$$

$$p = \frac{4\tilde{q}_m^2 + 3}{8\lambda}, \tag{2.97}$$

and $m \,\epsilon\, \mathbb{Z}^+$. Similar to the rigid pipe solution there additionally exists a zeroth mode with no cutoff frequency that is not found by equation 2.93. Cochrane gives this expression as a

series approximation as well from the power series of equation 2.92

$$\frac{\tilde{q}}{x} = \sqrt{\lambda}\left[1 + \frac{(\lambda-1)^2}{12\lambda} + \frac{(8\tilde{q}^2-3)(\lambda-1)^4}{480\lambda^2} + \ldots\right]. \tag{2.98}$$

The above two approximations for the modes can be solved for $\tilde{q}$ as a function of k for the higher order modes

$$\tilde{q} = \frac{\sqrt{\lambda(8\pi(n-1)(bk(\lambda-1)-\pi n+\pi)-3\lambda+6)-3}}{2(\lambda-1)}, \tag{2.99}$$

and for the zeroth mode

$$\tilde{q} = \frac{30\lambda^{3/2}\left(\left(\frac{b^2k^2\left(3\lambda^4-52\lambda^3-382\lambda^2-52\lambda+1\right)(\lambda-1)^4+7200\lambda^3}{7200\lambda^3}\right)^{1/2}+1\right)}{\tilde{b}k\,(\lambda-1)^4}, \tag{2.100}$$

both times taking the positive root as the solution. These both can be plotted as a function of ω to get the $\tilde{q}$ values that satisfy the characteristic equation 2.92. The solutions are plotted in figure 2.5.

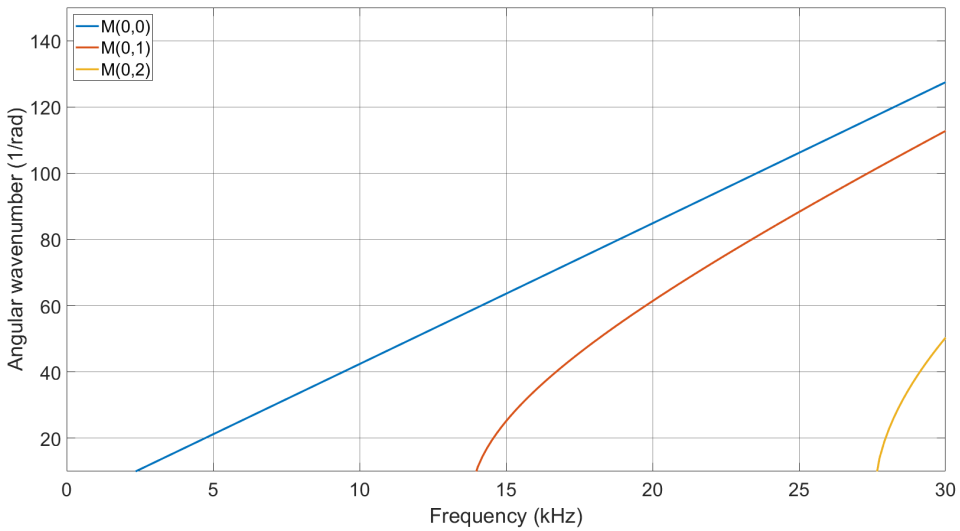

Figure 2.5: Modal angular wavenumber ($\tilde{q}$) solutions of a curved rigid pipe. Radius of curvature 1 m and pipe radius 2.6 m

Looking at figure 2.5, similar to the rigid pipe, there is one mode that always propagates

while the higher order modes all having a cutoff frequency. Using these $\tilde{q}$ solutions to the characteristic equation the phase and group speeds for the modes can be easily found using the relations in equations 2.89 and 2.90. This group speed is computed from these $\tilde{q}$ solutions and plotted in figure 2.6.

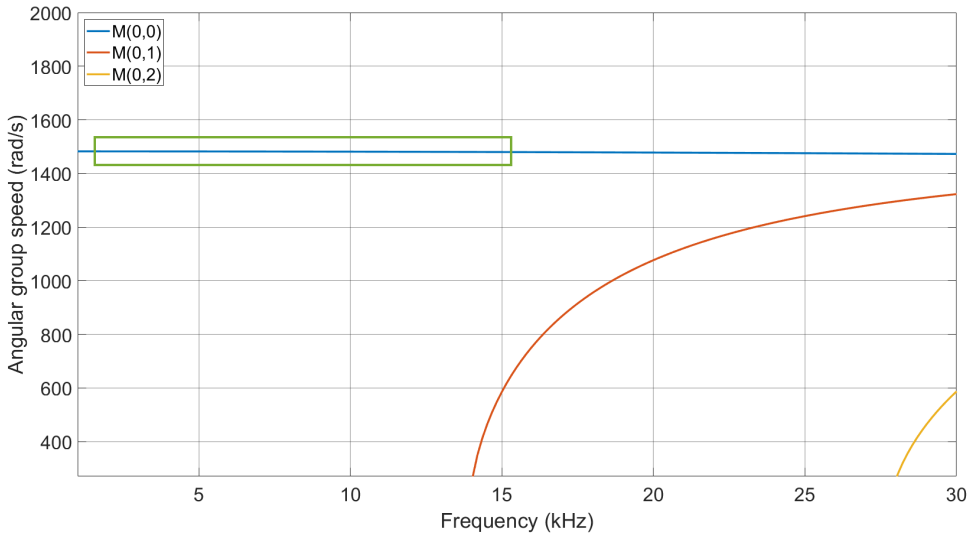

Figure 2.6: Modal group speed solutions of a curved pipe. The radius of curvature is 1 m with a pipe radius of 2.6 cm. Area in the green rectangle is plotted in figure 2.7

Looking at the group speed of the zeroth mode in figure 2.6 it is not clear if this first mode differs from the plain wave solution. Figure 2.7 zooms in on the the low-frequency sections to see the structure. While the speed of sound variation is minimal, this indicates that the curved pipe does cause of shift from the standard modal solutions. If the curve were to be exaggerated this effect would cause a higher deviation from the straight pipe solution.

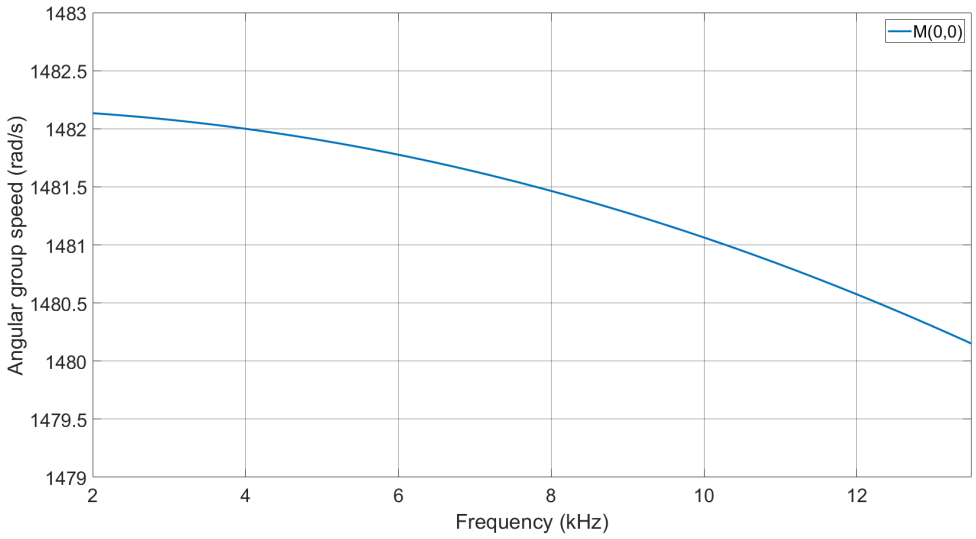

Figure 2.7: Group speed of zeroth order mode for a curved pipe. The radius of curvature is 1 m with a pipe radius of 2.6 cm.

CHAPTER 3

METHODS

3.1 Experimental setup

3.1.1 Hardware

The calibration setup consists of a copper pipe of outer diameter 169 mm and a thickness of 1 mm. The pipe is coiled into 4 coils of approximately 95 cm diameter. There are three 200mm openings along the top of the coil not including the pipe ends. The coil is suspended in an aluminum frame made of 1 inch extrusion on caster wheels for mobility. The pipe is attached to the frame through rubber spacers to minimize vibrations. The mechanical setup is shown in figures 3.1. The calibrations measurement use two icListen hydrophones manufactured by Ocean Sonics. The icListens are known as "smart hydrophones" as they have their amplification and digitization built into the system and do not require any extra hardware to function. The hydrophones used for calibration are RB9-ETHs which use the TC4059 element manufactured by Teledyne Reson.

The hydrophones are connected to the pipe using acetyl collars. These are sealed to the middle three openings using o-rings. Additionally there are o-rings that seal around the hydrophone elements. The whole system is filled with water until it begins to overflow on the pipe ends to ensure there are no air pockets. The water is filtered and deionized which minimizes impurities that could affect propagation. The hydrophones are connected using an Ethernet extension cable by Ocean Sonics to an icLink which acts as an Ethernet switch and allows the hydrophones to be configured through the network. The extension cables additionally carry a pulse-per-second (PPS) signal generated by the icLink which

Figure 3.1: 3D rendering of the hydrophone calibration system. The projector is located in the middle with the two hydrophones on either side.

synchronizes the hydrophone's sample clocks to within 100 ns.

The sound source is a Geospectrum M24-203-TI hydrophone element driven by a signal from a Tektronix AFG 3022B arbitrary function generator. To amplify the AFG's output, the output signal is connected through a TPA3220A Texas Instruments audio amplifier and a 12.5:1 toroid transformer. This applies approximately 52 dB of gain to the AFG's output. The function generator is connected to the same PPS source as the hydrophones and is configured to output the signal every 1 second pulse. To capture the transmitted signal, a Tektronix oscilloscope TBS 1052B is connected to the input signal. This oscilloscope is set to trigger using the same PPS signal so that the whole system is time-synchronized.

3.1.2 Path length measurement

While the path length can be estimated from the manufacturing specifications, knowing the exact path length for the propagation is needed for accurate speed of sound measurements. The geometry of this setup is shown in figure 3.2. The inside circumference between two sections is measured by running a thread through the tube and pulling it taut. The thread length is measured as ℓ. In addition to this, the height h above the system is measured in-situ.

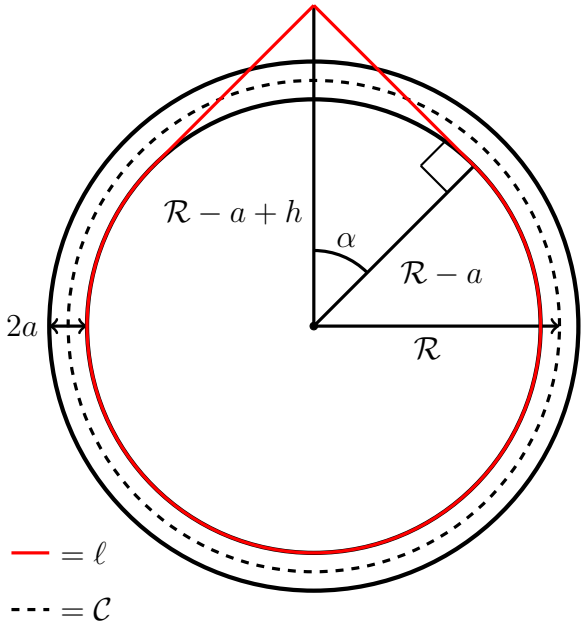

Figure 3.2: Diagram of the geometry for path length measurement.

The tube's outer diameter a is easily found by measuring the tube circumference $\mathcal{C}_{pipe}$

$$a = \frac{\mathcal{C}_{pipe}}{2\pi} \tag{3.1}$$

The propagation path length $\mathcal{C}$ is found by first calculating the non circular components of ℓ through

$$\delta^2 = (\mathcal{R} - a + h)^2 - (\mathcal{R} - a)^2 = h^2 - 2ah + 2h\mathcal{R}, \tag{3.2}$$

where 2δ is the total amount of excess on ℓ. Since both $\mathcal{R}$ and δ are unknown, more equations are needed to solve the system. These are

$$\ell = (2\pi - 2\alpha)(\mathcal{R} - a) + 2\delta \tag{3.3}$$

$$\cos(\alpha) = \frac{\mathcal{R} - a}{\mathcal{R} - a + h}, \tag{3.4}$$

where α is the angle defined in figure 3.2 and has units of radians. Equations 3.2 to 3.4 do not have an analytic solution but can be solved numerically for the radius $\mathcal{R}$ given the measurements of d, h and ℓ. The path length is given as

$$\mathcal{C} = 2\pi\mathcal{R}. \tag{3.5}$$

3.1.3 Calibration measurements

To perform calibrations, two hydrophones are placed as in figure 3.3. The projector is placed in the middle and connected to the amplifier. Using Tektronix's ARBexpress software the transmitted sweeps are created and loaded into the function generator. The sample rate for the generated sweeps is limited to 250 MS/s with a maximum length of 120 kS, where *S* refers to samples. This requires the template sweeps to be configured such that they are replayed at the correct settings. This is demonstrated in table 3.1. The template signal is transmitted by the function generator using pulse modulation, the pulse frequency f_{pulse} is chosen to ensure the correct sweep lengths.

Table 3.1: Sweep parameters used for calibration measurements

Desired Sweep			ARBexpress input (250 MS/s)			AWG
B (kHz)	f_c (kHz)	T (ms)	f_{start} (kHz)	f_{end} (kHz)	Samples (kS)	f_{pulse} (Hz)
1	1.5	4	10	20	100	250
1	1.5	8	20	40	100	125
⋮	⋮	⋮	⋮	⋮	⋮	⋮
1	14.5	4	140	150	100	250
1	14.5	8	280	300	100	125

The sweeps are all chosen to have a bandwidth B of 1000 Hz with a center frequency f_c varying from 1500 Hz to 14.5 kHz. The range is chosen to address the frequency gap between the current hydrophone calibration facilities at Ocean Sonics (10 kHz - 200 kHz) and the range of the Ocean Networks Canada's VLF calibration (0.01 Hz - 1000 Hz). The sweeps are performed at 4 ms and 8 ms. The hydrophones are configured to record at 64 kS/s packaging the data into 1-minute wave files. These files contain 60 sweeps which one signal occurring each second. The transmitted signal is captured concurrently by an oscilloscope triggered by the same PPS signal as the function generator. A capture of the signal is taken once per minute and used in the data processing.

3.2 Data Processing

To produce the calibration data, the wav files from the hydrophone are processed with the CSV file from the oscilloscope to get an estimate of the energy received by both hydrophones.

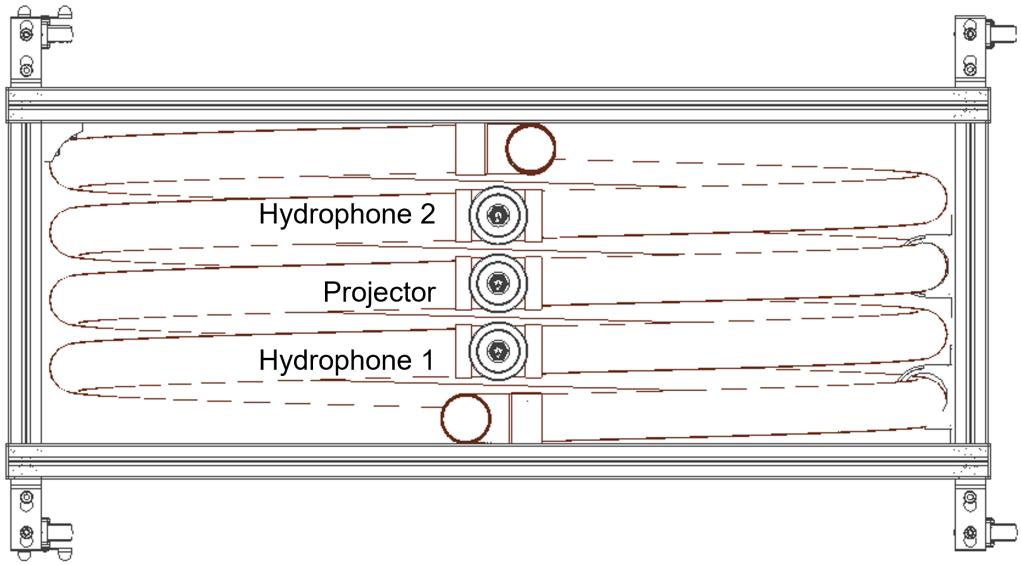

Figure 3.3: Top-down view of the hydrophone calibration system. The pipe is water filled with the end being open to air.

3.2.1 Pre-processing

The wav file is comprised of 60 individual sweeps each one corresponding to the start of the one second pulse. These 60 sweeps are averaged to produce one 1-s sweep signal for processing. This averaged signal is then filtered to remove unwanted spectral content. The signal is first low-pass filtered using a 6th order Butterworth filter and then high-pass filtered using a 2nd order Butterworth filter. Both filters are applied forward and backwards in time to double the amplitude gain while cancelling any phase change due to filtering. This method of filtering is non-causal and requires the data be previously collected and cannot be done in real-time.

After filtering, the wav data is resampled to match the sample rate of the oscilloscope. To perform the matched filter the two signals need to have the sampling rate. As the CSV sample rate is higher than that of the wav file, the wave file is interpolated at the new frequency. This increases the number of data points considerably making data manipulation difficult. The final step before match filtering is to truncate the wav data to only the first 200 ms of the entire 1 second record. After this point the received signal is dominated by reverb noise and does not contain any signals of interest. The cleaned hydrophone wav data is processed to extract the timing and energy information from the signals by

match-filtering.

3.2.2 Matched filtering

To determine the time offset between the transmitted signal and the received signal the two signals are cross-correlated.

3.2.2.1 Cross-Correlation

The cross-correlation of two sequences x_n and y_m is given by

$$R_{xy}(m) = E\{x_{n+m}{y_n}^*\} = E\{x_m{y_{n-m}}^*\}, \tag{3.6}$$

where $n = (-\infty, \infty)$, y^* is the complex conjugate of y and, E is the expectation value. The cross-correlation is implemented in MATLAB as the `xcorr` function. This function estimates the cross-correlation of two signals using the following expression

$$\hat{R}_{xy} = \begin{cases} \sum_{n=0}^{N-m-1} x_{n+m}y_n^* & m \geq 0 \\ \hat{R}^*(-m) & m < 0, \end{cases} \tag{3.7}$$

where N is the length of the x or y, whichever is larger. The output of `xcorr` is given as

$$C(m) = \hat{R}_{xy}(m - N), \quad m = 1, 2, ..., 2N - 1. \tag{3.8}$$

Functionally, this time shifts the two signals and then determines the correlation between each shifted signal. The cross-correlation is of length $2N - 1$ and is maximum when the two input signals are shifted such that they are maximally correlated. This is used to determine the time lag between source and received signals as the correlation will be highest when the source signal is shifted by the travel time.

When using the cross-correlation for timing, it is ideal that transmitted signal be non-repeating and distinct to time to have a narrow cross correlation peak and minimal side lobes. For hydrophone calibration, typically single frequency tones are transmitted since this allows for easy comparison of the energy received at a given frequency. However, since a tone is a periodic signal the cross-correlation output will not have a distinct peak and

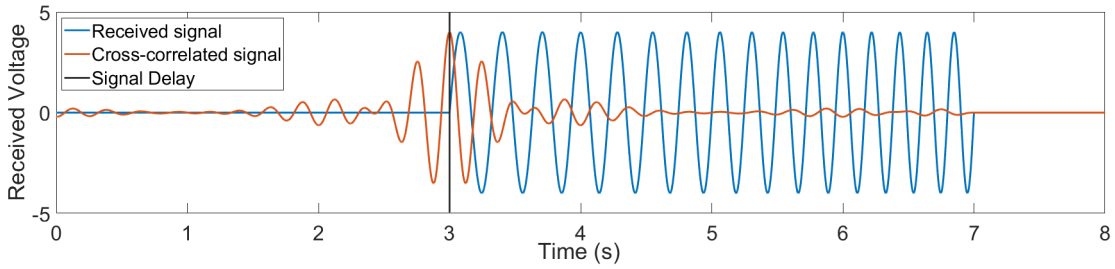

(a) Single frequency tone (5 Hz)

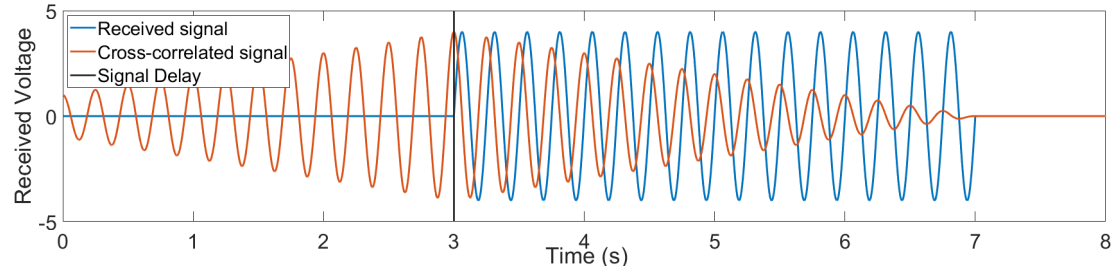

(b) Linear frequency sweep (4-6 Hz)

Figure 3.4: Comparison of the cross-correlation for two 4 s signals. The cross-correlation template is identical to the received signal starting at $t = 0$ s.

instead have large sidelobes. To ensure uniqueness, sinusoidal sweeps of small bandwidth (1000 Hz) are transmitted. Figure 3.4 compares the output of the cross-correlation of two signals of similar length and time delay. In figure 3.4, both the cross-correlation is maximum at the correct delay (in this 3 s) but the low bandwidth sweep has a much narrower peak due to the frequency modulation.

3.2.2.2 Normalization

While the standard cross-correlation determines the time-offset it does not convey any information about the energy of the received signal. This is due to the nature of how it is calculated by equations 3.6-3.8. To use the cross-correlation as a matched filter for calibration the output is normalized to relate the received energy of the hydrophone. To perform this normalization, first the energy of the known transmitted signal must be calculated. For an arbitrary finite-length signal $s(t)$ the energy $E_s(t)$ is given by

$$E_s(t) = \int_0^T |s(t)|^2 \, \mathrm{d}t, \tag{3.9}$$

where T is the length of s in time and $E_s(t)$ has units of u^2t (u being the units of $s(t)$). For a generic single-frequency sinusoidal signal with the form $s(t) = A\sin(\omega t + \phi)$ from

0 to T, the energy can be found as

$$E_s(t) = \int_0^T (A\sin(\omega t + \phi))^2 \ \mathrm{d}t = \frac{A^2}{2}\frac{\Big(\sin(2\phi) - \sin\big(2(\omega T + \phi)\big) + 2T\omega\Big)}{2\omega}. \quad (3.10)$$

If the tone is composed of a whole number n of cycles, the tone length can be represented as $T = n/f = 2n\pi/\omega$. Assuming the length is an integer number of cycles, equation 3.10 reduces to

$$E_s(t) = \frac{A^2}{2}T, \quad (3.11)$$

where A is the amplitude of the tone and T is the signal length. In equation 3.11 the energy of the signal does not depend on the frequency or the phase simply the amplitude and length. Due to this, it is possible to define the energy of the linear sweep to be the same as a single frequency tone of same amplitude and length.

Using equation 3.11, the transmitted signal s_{tr} is energy normalized by dividing by the square root of its energy

$$\hat{s_{tr}} = \frac{s_{tr}}{\sqrt{E}} = \frac{s_{tr}}{A\sqrt{T}}\sqrt{2}, \quad (3.12)$$

where $\hat{s_{tr}}$ now has units of $[1/\sqrt{s}]$. Assuming the received signal has units of volts the cross-correlation C between this energy transmitted signal and the received signal s_{rc} now has units of $[V/\sqrt{s}]$). The cross-correlation is scaled such that the output units match the received signal. These scale factors are determined through unit analysis and empirical testing. There are three units of interest that can be extracted from the cross-correlation: the received signal energy E_{rc}, the received signal voltage V_{rc}, and the power spectral density (PSD) of the received signal. Each one requires their own scale. Since the cross-correlation in equation 3.7 is the sum of the product of the two signals, the cross correlation is additionally scaled by the number of samples N_{tr} of the transmitted signal as an increase the number of data points will add to the total value. This gives the scaled correlation

$$\hat{C} = \frac{C}{N_{tr}}. \quad (3.13)$$

Since the sample rate $f_s = N_{tr}/T$, this scaling also takes into account changes in the sample rate between measurements.

To scale for energy, the cross-correlation is squared so that it has units $[V^2/s]$. Recall

that the units of signal energy are defined in equation 3.9 are $V^2 \times s$ this requires that $\hat{C}$ is scaled by the transmitted signal length T^2 giving

$$E_{rc} = \hat{C}^2 T^2. \tag{3.14}$$

From the expression for received energy, the received voltage can be found using the expression for signal energy in equation 3.11. To scale to volts, $\hat{C}$ is multiplied by the square root of the signal length. Additionally since the energy of the signal has a factor of 2, the voltage scaling includes $\sqrt{2}$ such that

$$V_{rc} = \hat{C}\sqrt{2T}. \tag{3.15}$$

By calculating the expressions 3.14 and 3.15, the exact energy or amplitude of the received signal can be found even when there is a large amount of noise present. This process is known as matched filtering. This is shown in figure 3.5 where two linear sweeps of the same characteristics with different amplitudes and delays are added together to simulate two signals interference. The matched filter both represents the individual signals as distinct peaks in time but also reproduces their input voltages despite the presence of noise.

The effect of the matched filter on noise is best seen when comparing the power spectral density (PSD) of the received signal to the PSD of the filtered signal. To scale the matched filter for the PSD a factor of the time-bandwidth product is added to account for the spectrum processing. The scaling is

$$PSD_{rc} = V_{rc}\sqrt{2BT}, \tag{3.16}$$

where V_{rc} is the scaled voltage correlation from equation 3.15 and B is the bandwidth of the sweep. The PSD of the scaled matched filter is calculated and compared to the PSD of the raw received signal in figure 3.6. In addition a bandpass filter is applied to the received signal with a pass band equal to the sweep's bandwidth. In figure 3.6 the spectral is preserved within the sweep's bandwidth with both filters. The matched filter however has much lower noise rejection compared to the generic filtering. This effectively adds

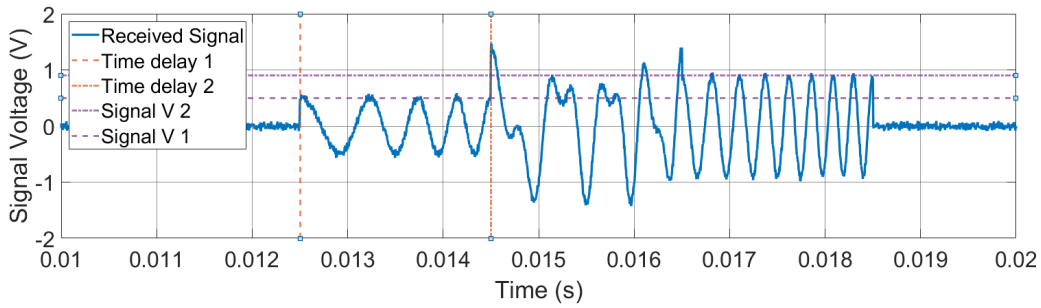

(a) Raw received signal

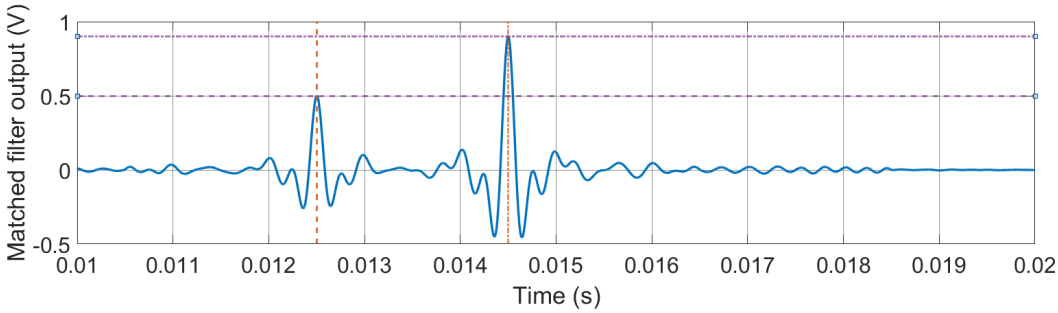

(b) Matched filtered signal

Figure 3.5: Effect of the normalized matched filter on interfering signals. Raw signal (a) is comprised of two identical (with different amplitude) that are interfering. This is compared to the matched filter output (b).

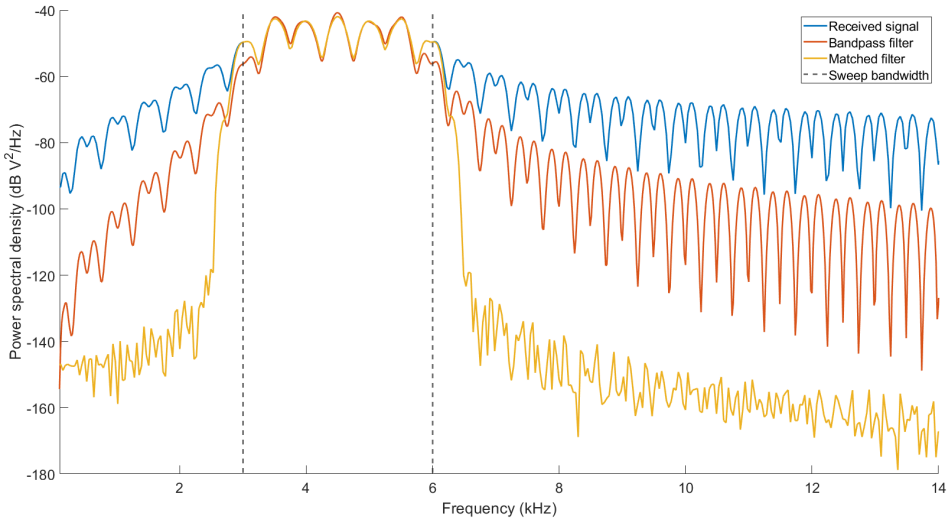

Figure 3.6: Power spectral density of a linear sweep (3-6 kHz) with an applied matched filter and bandpass filter. Bandpass filter's pass band is the same as the sweep's bandwidth.

processing gain to the system increasing the signal to noise ratio.

3.2.3 Post-processing and calibration

The voltage and energy of the two hydrophones calculated through matched filtering are then processed to extract produce the calibration curve. First, to ease future processing, the matched-filtered data is packaged into MATLAB data structures and saved. This is to prevent the need to re-filter individual measurements during data analysis. This filtered data is used to produce two outputs for the system: the time of first arrival t_d and hydrophone sensitivity $\mathcal{S}_T$.

3.2.3.1 Time Delay and Dispersion

The theory in chapter 2 suggests that the speed of sound in the calibration system will not only be slower than the speed of sound of the liquid (even the plain wave mode) but will vary with frequency according to a dispersion relation as in figure 2.3. The matched filtered data is used to determine the speed of sound for each test frequency. As each measurement is done of a sweep of non-zero bandwidth and represents a range of frequencies, the centre frequency is chosen as the representative point. The peak of the matched filter represents the point of highest correlation and represent the time of first arrival t_d. Taking this time delay and the measured path length $\mathcal{C}$ from section 3.1.1 gives an estimate for the sound

speed

$$c(f) = \mathcal{C}/t_d, \tag{3.17}$$

where $c(f)$ is the measured frequency dependent sound speed.

3.2.3.2 Calibration

From the results in section 3.2.2 the amplitude of the matched filter corresponds to the energy (or voltage) received at the time delay. This maximum value from the filer which corresponded to the first arrival is the energy of the received signal. This is used to find the sensitivity of the hydrophones at various frequencies. The process uses the same principle for the method references in free-field from IEC 60565-1:2020. By comparing the received energies from the test unit and the reference unit, the sensitivity is calculated. The method requires that the reference unit be externally calibrated with a known sensitivity at the test frequencies. For the experiment this reference is found from the element calibration from Teledyne Reson, the manufacturer of the hydrophone. The pressure measured by the reference hydrophone P_r

$$P_r(f) = 10\log\left(\frac{E_r(f)}{T}\right) - \mathcal{S}_r(f), \tag{3.18}$$

where E_r is the energy found through matched filtering and $\mathcal{S}_r$ is the externally calibrated sensitivity of the reference hydrophone in units of dB re $V/\mu Pa$. Note that the energy and sensitivity are frequency dependant. The voltage referred to in the units of sensitivity refer to the root-mean-squared (RMS) voltage of the signal. Comparing this known pressure to the measured energy of the test hydrophone E_t the sensitivity of the test hydrophone is found by

$$\mathcal{S}_t(f) = 20\log\big(E_t(f)T\big) - P_r(f). \tag{3.19}$$

This gives specific sensitivity values at various input frequencies. The sensitivities at each frequency are compiled into one calibration curve and compared with previous measurements to qualify if the waveguide method produces equivalent results.

CHAPTER 4

RESULTS

Multiple data collection runs were performed using icListen units to estimate the unit sensitivity as well as the dispersion curve of the system. The details for the runs to characterize the RB9-ETH type hydrophone with the Reson TC4059 element are given in table 4.1. The data is broken into runs corresponding to the hydrophones position and sweep length T.

Table 4.1: Data series used for RB9-ETH calibration measurement

Run	Date	Unit S/N	Unit position	B (kHz)	T (ms)	f_{start} (kHz)	f_{end} (kHz)
1	2022-12-11	6465	P1	1	4	1.5	14.5
2	2022-12-11	6466	P1	1	4	1.5	14.5
3	2022-12-11	6465	P2	1	4	1.5	14.5
4	2022-12-11	6466	P2	1	4	1.5	14.5
5	2022-12-11	6465	P1	1	8	1.5	14.5
6	2022-12-11	6466	P1	1	8	1.5	14.5
7	2022-12-11	6465	P2	1	8	1.5	14.5
8	2022-12-11	6466	P2	1	8	1.5	14.5

4.1 Path length

In section 3.1.2 a method for determining the path length between the hydrophones is proposed. The lengths were measured with the results and corresponding path lengths tabulated in table 4.2.

The results in table 4.2 show that the distance between the two paths differs by 2 cm.

Table 4.2: Measured and calculated data for the path lengths. The difference between the two paths is 2 cm

	Measured length ℓ (mm)	Height h (mm)	Radius R (m)	Path Length $\mathcal{C}$ (m)
Centre-P1	290.0	50	0.484	3.05
Centre-P2	289.3	50	0.483	3.03

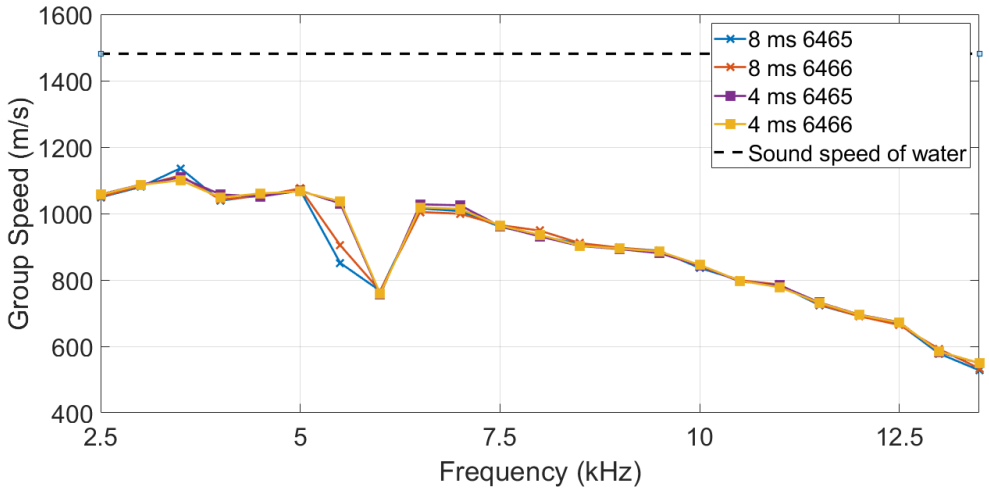

Figure 4.1: Position 1 group speed dispersion of RB9 type hydrophones

Assuming that the speed of sound is in the order of 1000 m/s this corresponds to a time difference in the order of tens of microseconds. This is large enough to be detected by the hydrophone sampling at 64 kS/s as the sampling period is 15.625 μs.

4.2 Dispersion

As the path lengths between P1 and P2 are different the dispersion is calculated separately for both positions and plotted in figures 4.1 and 4.2. Both plots show a decrease in group speed from around 1000 m/s to 500 m/s across the bandwidth. The plots show that despite the path lengths being similar the shapes of the dispersions are distinct. The most striking differences are the large nulls in sound speed at 6 kHz in position 1 and at 3.5 kHz, 6 kHz and 9 kHz in position 2. These are areas where the sound speed drops to a much lower value than the surrounding points. These nulls are the same regardless of hydrophone serial number indicating that the characteristics observed are related to the propagation paths only.

Investigating these sound speed drops, the normalized cross-correlation envelops for the

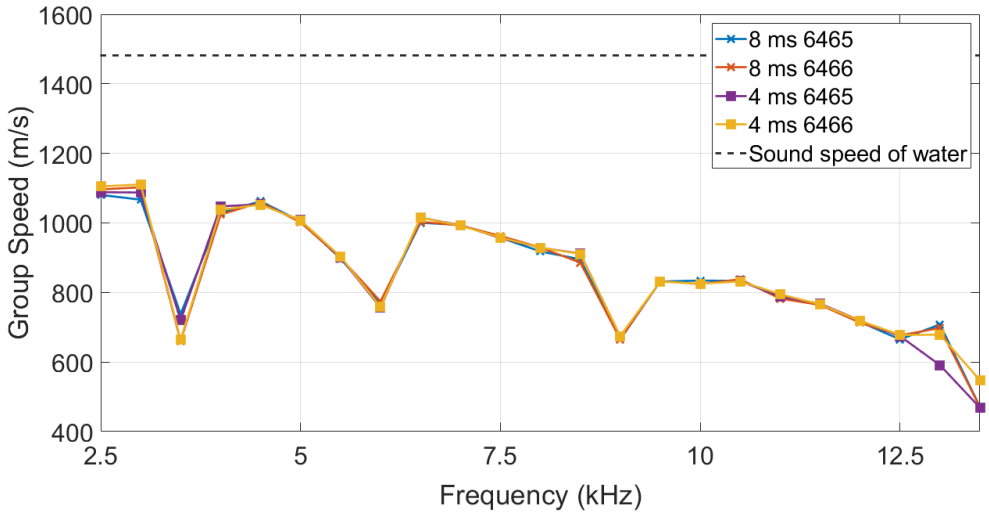

Figure 4.2: Position 2 group speed dispersion of RB9 type hydrophones

6 kHz null as well as the surrounding frequencies (5.5 and 6.5 kHz) are plotted in figure 4.3 to compare their shapes. The maximum correlation for 6 kHz occurs at 4 ms, while the peaks for the other sweeps fall between 3 and 3.5 ms. In figure 4.3, the 6 kHz sweep has has two peaks. One at 2.7 ms and the higher one at 4 ms. Between these two peaks there is a clear dip in the matched filtered data at 3.1 ms. This decrease in energy corresponds to where the expected peak for 6 kHz would occur. Figure 4.3 suggests that at the null

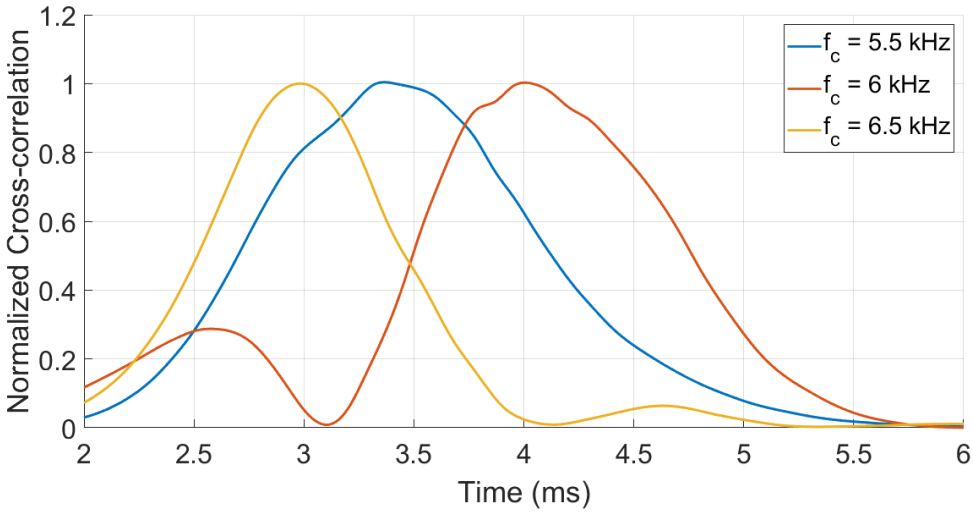

Figure 4.3: Envelope of the normalized matched filtered energy for three frequency sweeps in position 2. $T = 4$ ms

frequencies there is a process that causes the sweep to be dissipated. This is also shown in

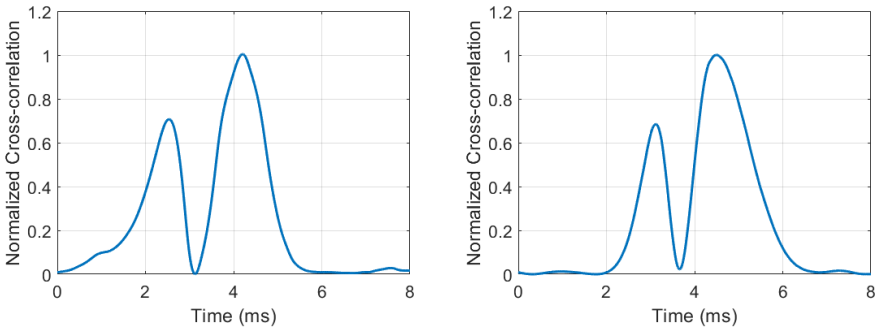

(a) Sweep 3 kHz to 4 kHz (b) Sweep 8.5 kHz to 9.5 kHz

Figure 4.4: Envelope of normalized matched filtered energies at the two dispersion null locations unique to position 2 (3.5 kHz and 9 kHz). $T = 4$ ms.

figure 4.4 where at both 3.5 kHz and 9 kHz there is a visible drop in energy between two larger peaks. The two positions share nulls at 6 kHz while the additional drops occur only in position two. This suggests that there is some other process that is unique to position 2 causing the drop at 3.5 and 9 kHz. Even though there are large changes in sound speed, The overall pattern is consistent between multiple hydrophones and sweep lengths. This implies that calibration measurements should still be possible since the reference and test hydrophones will measure the same pressure field. Considering the overall shape of the dispersion, both curves differ substantially from the predicted dispersion from figure 2.3. The predicting dispersion is flat across the bandwidth 2.3 kHz - 13.5 kHz at 500 m/s. The measured dispersion has an overall decrease in sound speed over the bandwidth. The difference between the theoretical dispersion and the measured data will be discussed in chapter 5.

4.3 Calibration

Calibration measurements are done on the icListen hydrophones in position 1 and position 2 at both 4 ms and 8 ms for the sweep length. The longer sweep length is expected to have high sensitivity accuracy as there is more energy dispersed into the pipe which should give better energy estimates. The calibrations with a 4 ms sweep are shown in figure 4.5. The reference was chosen as unit 6466 and the test unit as 6465. A known sensitivity of unit 6465 provided by the element manufacturer Reson is additionally plotted along with their reported uncertainties (± 1 dB). As the external calibration data does not contain

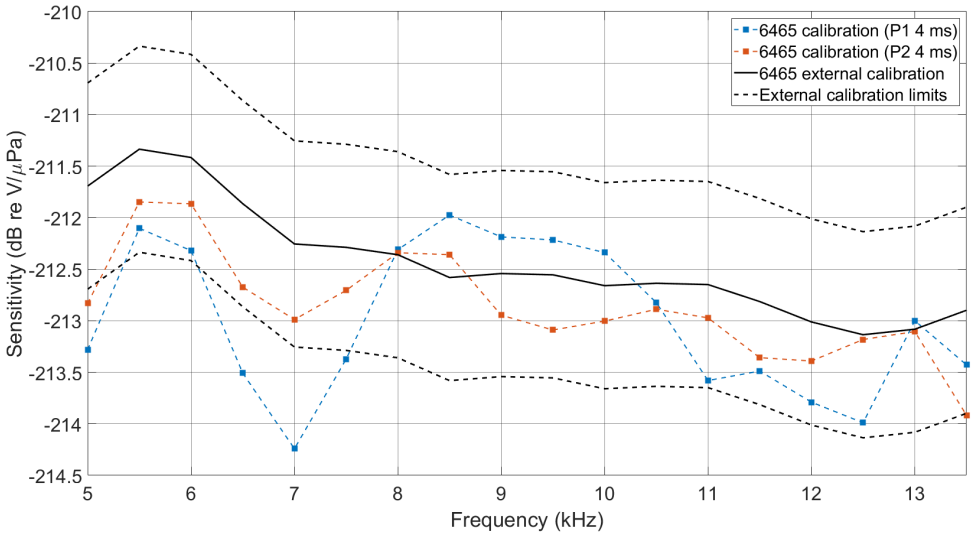

Figure 4.5: Measured sensitivity of unit 6465 with $T = 4$ ms. Data is compared to an external calibration of unit 6465 done by Teledyne Reson

measurements for below 5 kHz the calibrations are reported between 5 kHz and 13.5 kHz.

Looking at the calibrations in figure 4.5 both curves are generally within the uncertainty given by Reson. The calibration done in position 2 agrees more with the external results while the position 1 measurement is outside the limits between 6.5 and 7.5 kHz. The calibrations done using the longer 8 ms sweeps are plotted in figure 4.6. Similarly, the findings using longer sweep lengths in position 1 and position 2 are both generally within the limits provided by Reson. The position 2 measurement once again produces a better match while the position 1 measurement is outside the limits between 6.5 and 7.5 kHz.

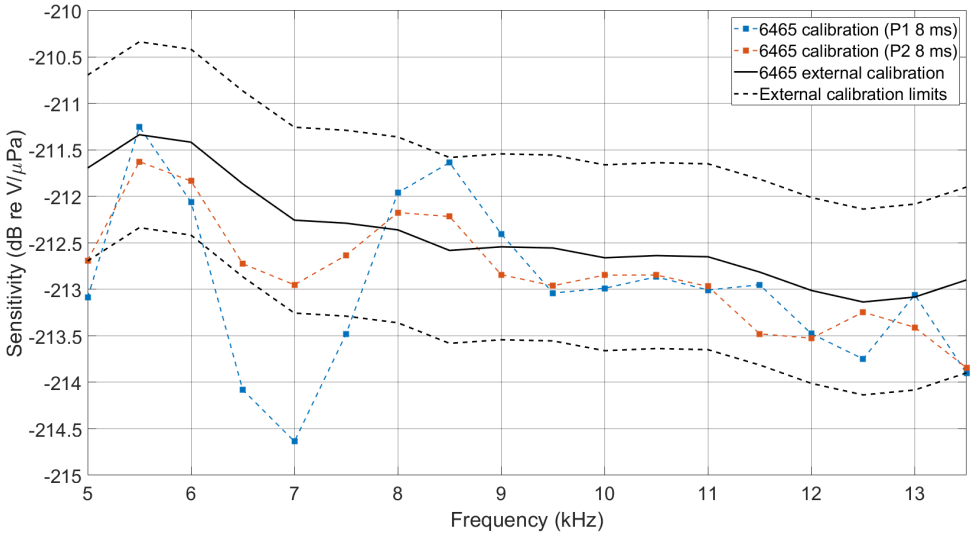

Figure 4.6: Measured sensitivity of unit 6465 with $T = 8$ ms. Data is compared to an external calibration of unit 6465 done by Teledyne Reson

CHAPTER 5

DISCUSSION

The results in chapter 4 give an example of calibration measurements using the developed calibration system. The analysis is focused on characterizing and validating the system with the theory presented in chapter 2 as well as processing the data to achieve a low-frequency sensitivity curve. The following chapter will first discuss the dispersion curve and how it deviates from the theory, then discuss the sensitivity measurement. Finally, future improvements to the system are proposed.

5.1 Group speed dispersion

The group speed dispersion measured for the calibration system differs from the dispersion predicted by the theory in section 2.4. This is evident in figure 5.1 where the theoretical dispersion modes are plotted along an average of the measured dispersion. There are three considerations that must be discussed to understand how the theory differs from the experimental data: the points of lower group speeds denoted as "nulls", the decrease in group speed with frequency, and the differences in group speed magnitudes. All three will be addressed individually in the following sections.

5.1.1 The sound speed nulls

The most noticeable differences between the theoretical group speed of a 5.5 cm copper pipe and the measured group speed are the regions of decreased sound speed at 6 kHz for both positions 1 and 2, and 3.5 and 9 kHz in only position 2. Both the position 1 and

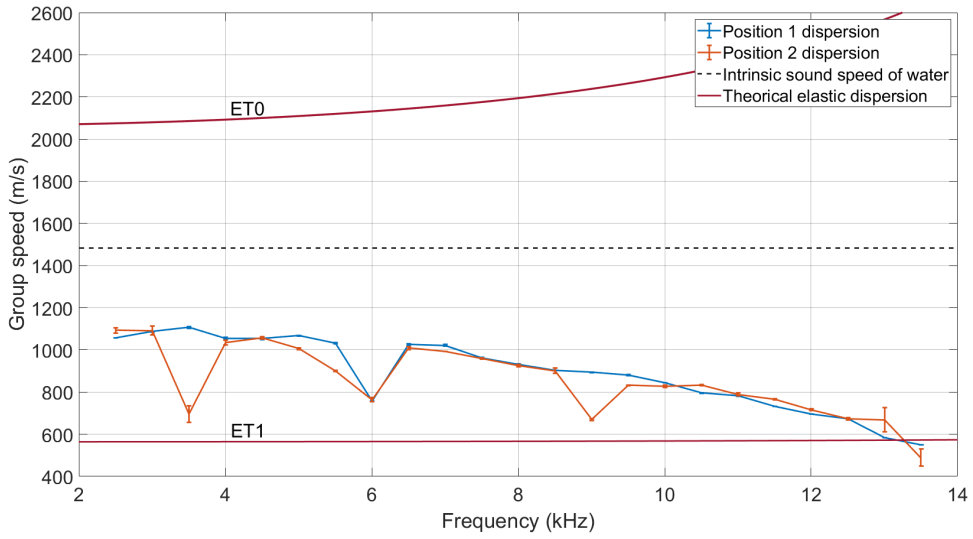

Figure 5.1: Measured group speed in positions 1 and 2 compared against the theoretical sound speed

position 2 dispersion are plotted in figure 5.1. These nulls are investigated to determine the cause of discrepancy.

One possibility is that there is a process that is suppressing a wavefront (either ET0 or ET1 to determined later) and what is being measured is either reverberation or a slow moving mode. If the measured signal is reverb and not a separate mode then the points where the measured speed drops must be an underestimate. This is because the assumed path length ($\sim$3 m) is no longer correct. To investigate this, first an average interpolated group speed is found for 2.5-13.5 kHz by removing the frequencies at which the nulls occur. This new group speed is plotted in figure 5.2. Using this idealized group speed the travel distance of individual matched-filter peaks can be investigated. This is done on two frequencies 6 kHz and 6.5 kHz. As shown in the diagram in figure 3.3, the first reflection should occur at the water-air interface at the pipe ends. As this is a pressure release boundary most of the sound energy should be reflected back into the system causing reverberation. This boundary is 3 m beyond the hydrophone locations so a measured reverb signal will occur 6 m after the direct path (9 m of total travel distance). To determine if the reverb location is correct the matched filtered voltage envelope is plotted in figure 5.3 as a function of propagation distance for two frequencies (one with the null and the other without). Looking at the 6.5 kHz sweep the highest correlation occurs at the direct

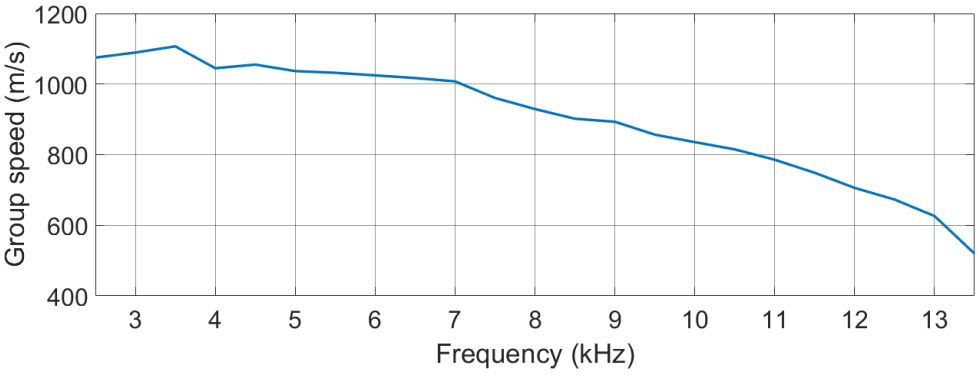

Figure 5.2: Idealized group speed of calibration pipe. Group speed measurement from figure 5.1 is average without the null frequencies and then interpolated.

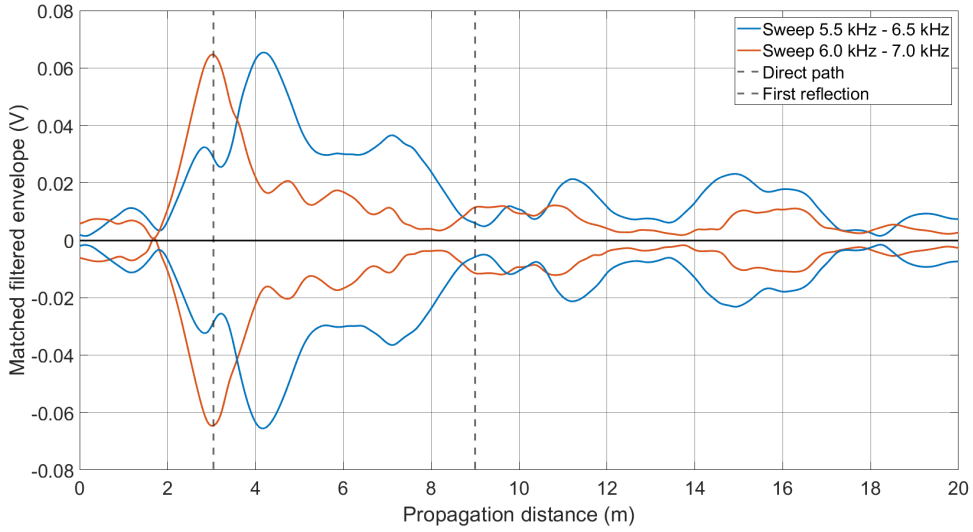

Figure 5.3: Calibration signal propagation against travel length in position 1. The sweep 5.5 kHz - 6.5 kHz is a null frequency compared against 6 kHz - 7 kHz which is not.

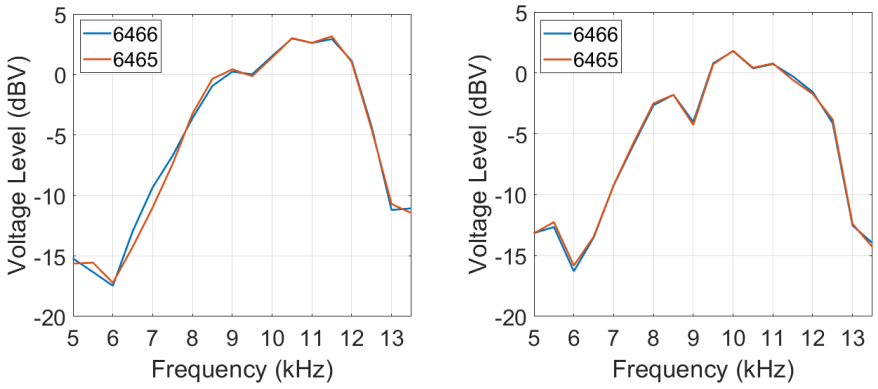

(a) Position 1 (b) Position 2

Figure 5.4: Measured received voltage level (dBV) from the normalized matched filter. 8 ms sweep length comparison between hydrophones 6565 and 6466

path with a number of smaller peaks extending out to 20 m of propagation distance. Of particular interest is the peak at 9 m which would be the location of the first reflection. This indicates that the speed of sound is correctly predicted for this frequency. However, when looking at the 6 kHz sweep the source of the individual peaks is less clear. The highest correlation peak occurs at 4.1 m which does not correspond to any geometric paths. There are additionally no obvious correlation peaks at 9 m for the first reflection. This shows that if the speed of sound was an underestimate the received signal is not entirely reverberation. The received voltage of both peaks in figure 5.3 have similar levels so the signal that is being measured is a real wave-packet. If the 6 kHz signal were simply being suppressed and no other signal was propagating it would be expected that there would be no strongly correlated peaks in the data. Figure 5.4 shows the range of peak voltage levels measured for different frequencies. The figure shows that at the null frequencies there are visible decreases in measured voltage compared to the surrounding frequencies. This decrease is not large enough however to argue that any measured signal is random noise fluctuations and not a propagating wave-packet. This shows that more likely a separate mode is being excited when the main mode is suppressed. A detailed discussion of the possibility of other propagating modes is found in section 5.1.3.

Now to consider why the 6 kHz sweep is damped and not propagating. To do this, the wavefield inside the tube is simulated for each frequency. Using the idealized group speed from figure 5.2, the mode characteristic X_{0m} is found using equation 2.32. With this

:

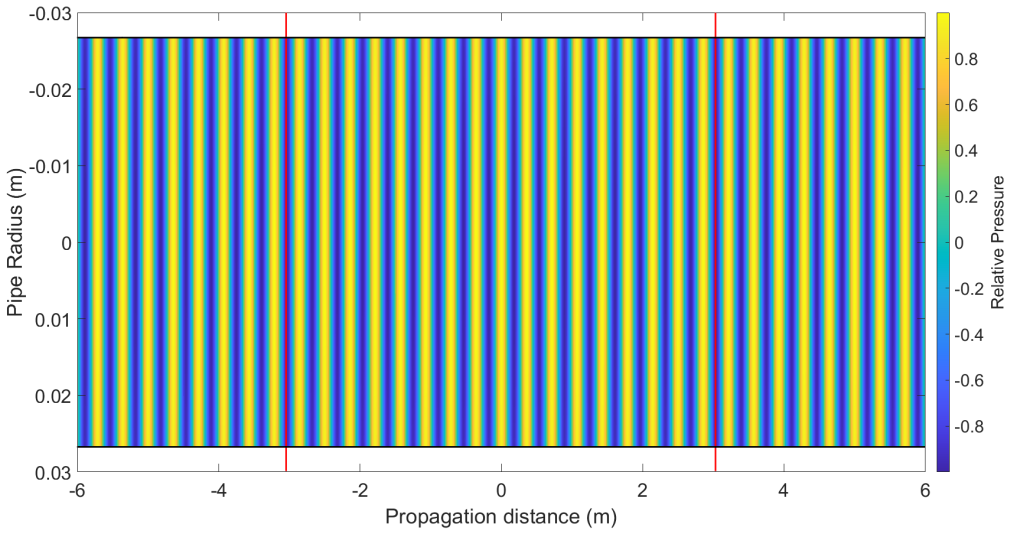

Figure 5.5: Simulated waveform at 6 kHz using idealized sound speed. Projector is placed at $r = 0$ and with the two hydrophone positions indicated by the red lines.

characteristic value the entire pressure field can be plotted at steady state using equation 2.22

$$p(r, z, t = \infty) = \sum^{m} p_{0m} J_0 \left(r \frac{X_{0m}}{b} \right) e^{i(q_{0m} z)}. \tag{5.1}$$

Since there is only one mode measured in the dispersion, the wave field can be found without the need to compute the constant p_{0m} and instead have the pressure field be a relative value. The wave-field is plotted in figure 5.5. Looking at the simulated field, the hydrophone positions correspond to areas of large negative pressure. At this location there is an expansion of volume due to the coupling between the hydrophone and pipe. This would cause the 6 kHz signal to be damped due to the expansion chamber effect. If this were to be the case, then at other frequencies the hydrophone position would not correspond to areas of large pressure magnitude. To test this, the wave-forms are plotted for all measurement frequencies. As the pressure field is nearly constant in the radial direction, the field can be plotted at $r = 0$ for all frequencies as is done in figure 5.6.

Looking at the wave propagation in figure 5.6 there are multiple frequencies that correspond to large pressure levels. These include 3, 7.5, 10, and 12.5 kHz. For the expansion chamber theory to be correct, the damping would have to be quite sensitive for the hydrophone position to only occur at the minimum voltage. As the measurement of the

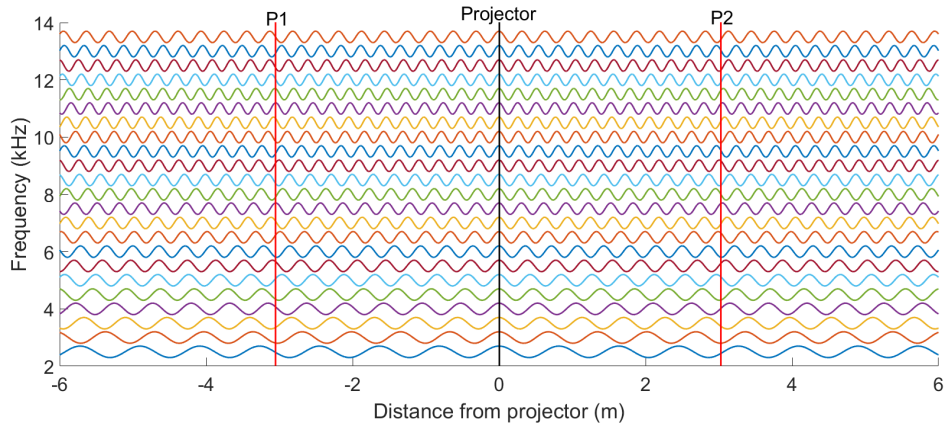

(a) Full pipe length

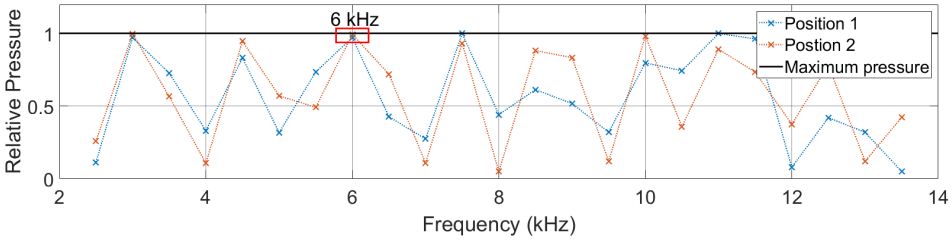

(b) Cross-sectional slice at position 1 and position 2

Figure 5.6: Propagation of elastic modes using the idealized sound speed. Frequency of individual mode is given by the y-axis value.

propagation distance has some associated error it could be the case that the proper path length is shifted slightly based on measurement. Additionally since the initial sound speed estimates are based on this propagation distance through equation 3.17, any errors in time and distance measurement would be compounded.

To address this, consider a frequency dependent group speed c_g measured by the methods from section 3.2.3. Using the relation between group speed and characteristic value in equation 2.32, the expression for the characteristic value is

$$X_{0m} = kb\sqrt{1 - \left(\frac{c_g}{c}\right)^2}, \tag{5.2}$$

where k is the plain wavenumber, b is the pipe's inner diameter and c is the intrinsic sound speed of the liquid. Recalling the Pythagorean expression in equation 2.20 the modal wave number (q_{0m}) can be calculated as

$$q_{0m} = \sqrt{k^2 - k^2\left(1 - \left(\frac{c_g}{c}\right)^2\right)} = k\frac{c_g}{c}. \tag{5.3}$$

For the expansion chamber effect to be considered, an odd integer number of half wavelengths need to propagate between the projector and the hydrophone. Mathematically if the propagation path between the projector and the hydrophone is $\mathcal{C}$ then the requirement is

$$\frac{c_g}{c}k\mathcal{C} = \frac{(2n+1)\pi}{2}, \qquad n \in \mathbb{Z}^+. \tag{5.4}$$

Since c_g is also a function of $\mathcal{C}$ the expression reduces to

$$\frac{\mathcal{C}^2\omega}{t_d c^2} = \frac{(2n+1)\pi}{2}, \tag{5.5}$$

where t_d is the delay time found by cross-correlation. The relation in equation 5.5 gives an expression for $\mathcal{C}$ as a function of frequency given fixed t_d and n. This relation is plotted with increasing n in figure 5.7 for the calibration frequencies. Figure 5.7 demonstrates that there is only one frequency within the test range that corresponds exactly to a given projector distance.

While this analysis does not prove that the null at 6 kHz is due to an expansion chamber

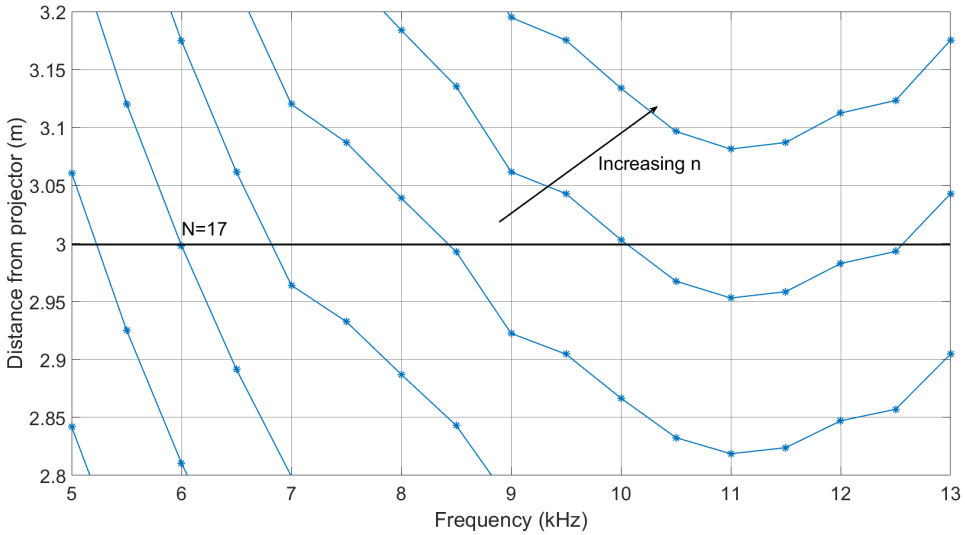

Figure 5.7: Locations for 1/2 wavelength distances from projector at varying frequencies and increasing n values. The predicted distance from the projector is given by the black line.

effect, the above demonstrates that for a given projector distance there is, in general, only one frequency that is precisely n half wavelengths away. Due to the uncertainty in the measurement of both $\mathcal{C}$ and t_d, the correct values could be ones that require 6 kHz to be damped.

Now, turning attention to the nulls unique to position 2 (3.5 and 9 kHz). Since they do not appear in position 1, whatever process is causing these nulls must be related to the physical system between the projector and position 2. One possibility is the mounting brackets that attach the tube to the outer frame. To keep the system upright, four mounting brackets are placed along the pipe, these are modified pipe clamps. To attempt to minimize the coupling of the pipe into the frame, absorptive material in placed between the clamp and the pipe. These clamps are placed throughout the outer edge of the frame however there is only one that is in the direct path between the projector and the hydrophones. The other three lie outside the direct propagation path beyond the hydrophone positions. The simulated propagation for 3.5, 6 and 9 kHz are plotted in figure 5.8. The propagation waveforms show, much like the 6 khz case, that there is a pressure maximum for 3.5 and 9 kHz but not at 6 kHz around the location of the bracket. As this bracket is mechanically connected to the pipe this produces a local area of high stiffness where the pipe cannot bulge as is

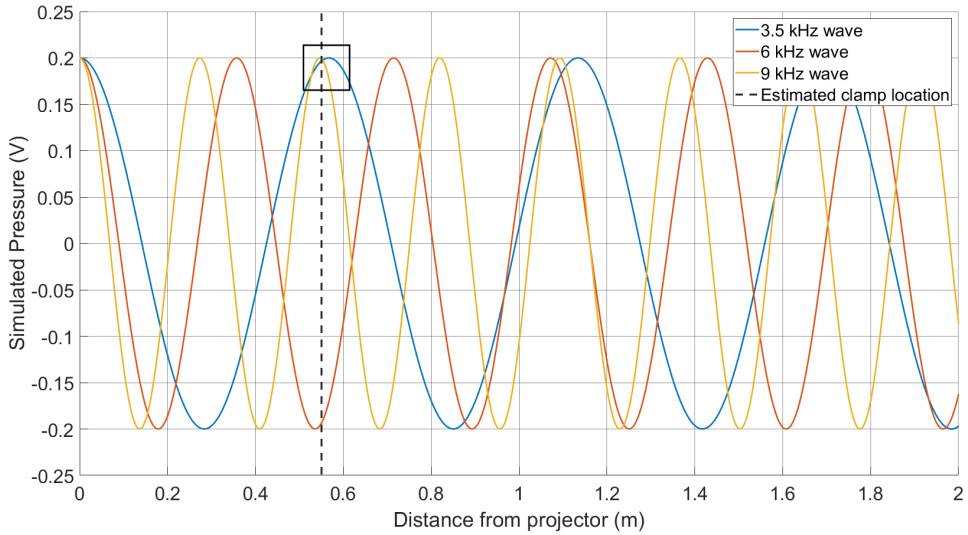

Figure 5.8: Simulated frequencies for the position 2 nulls. Estimated location of the mounting bracket is plotted in black.

predicted by the model. This stiffness will cause the mode to no longer propagate since the system cannot support the compliant wave. If the above is correct, it is expected that moving the bracket locations will cause these two nulls to disappear. It is suggested for future calibration work on this system to have the mounting points all near the end of the pipe to not effect the direct propagation path.

5.1.2 Decrease in group speed over frequency

The measured dispersion in figure 5.1 shows a continuous decrease in group speed over the measured bandwidth. The decrease is not observed in the theoretical elastic dispersion. Recalling analysis developed in section 2.6, it was found that the addition of pipe curvature along the propagation path would cause a decrease in group speed with increasing frequency. Taking this calculated data for the rigid mode and performing a curve-fit indicates that within the region of 2.5-13.5 kHz there is a a quadratic decrease in group speed with increasing frequency. Performing the regression on the idealized dispersion from section 5.1.1 yields a quadratic relation as well. The two fits are shown in figure 5.9. While both regressions indicate a quadratic relation with group speed, the respective magnitude of the decreases is different.

First, consider how the analysis in section 2.6 differs from the elastic theory. The dispersion from section 2.6 assumes rigid boundary conditions with square pipe walls.

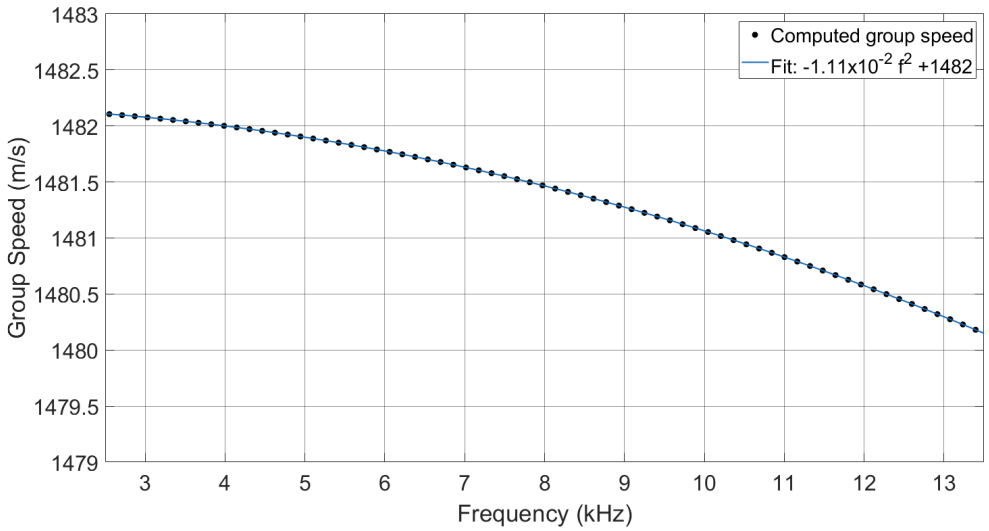

(a) Theoretical

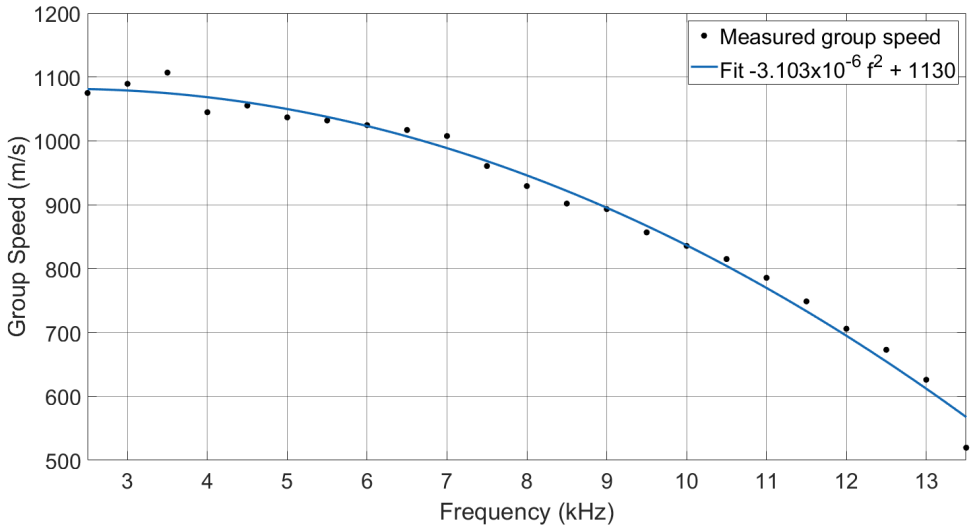

(b) Measured

Figure 5.9: Quadratic curve fit of group speed dispersion for measured sound speed and theoretical rigid pipe.

Square pipe walls are a consequence of the geometric setup presented in figure 2.4. This geometry does not allow for a circular cross-section as the boundary condition on r is restricted to $\tilde{b}$ and $\tilde{d}$. This was done in order to solve the Helmholtz equation in spherical polar coordinates having $\hat{\theta}$ be the propagating direction. While this greatly simplifies the calculation it does not reflect the calibration system. However, since the propagation speed in a straight square pipe and a straight circular pipe in the zeroth mode is the same, the simplification still gives insight on how propagation is affected by curvature.

Using the curved pipe results, it can be argued qualitatively that the group speed decrease observed in the calibration system can also be explained by the curvature of the calibration pipes. The difference in magnitude seen in figure 5.9 is likely due to the differences in the boundary conditions as the theory assumed rigid walls. From the results in section 2.4 it is known that the inclusion of elastic boundary conditions causes a large change in the dispersion characteristics of the system.

To confirm this, another treatment of the simplified geometry with elastic walls will demonstrate if the addition of realistic boundaries causes a larger decrease. Additionally it could be possible to restate the geometry of the curved pipe in toroidal coordinates to express curved propagation with a circular cross-section. Unfortunately the Helmholtz equation is not separable in those coordinates so the same differential equation techniques cannot be used (*Moon and Spencer*, 1952). A numeric study would be needed to express the full elastic solution in the curved regime.

5.1.3 Magnitude of the group speed

The results from the measured group speed do not line up well in magnitude with the predicted speed for either ET0 or ET1. The measured group speed is between 1100 m/s at 2.5 kHz and 550 m/s at 13.5 kHz. From the discussion in section 5.1.2 it is assumed that this decrease is entirely due to the pipe curvature and the true low-frequency group speed is 1130 m/s as the maximal value of the fit parabola in figure 5.9b. This value is between the predicted group speed results of 2071 m/s for ET0 and 564 m/s for ET1. It is also clear from the plot of the matched-filter output in figure 5.3 that there is only one mode that propagates with appreciable amplitude. If both ET0 and ET1 were propagating, there would be two detectable peaks in the match filter which is not the case.

As only one mode propagates the question is what is being detected. Even though the

Table 5.1: Modal amplitudes of different test frequencies. The amplitude of the piston source ϕ_0 is given as 1 μPa

Frequency (kHz)	3	6	9	12
ET0 (μPa)	0.41	0.40	0.39	0.34
ET1 (μPa)	0.49	0.49	0.48	0.45

system supports two axisymmetric modes, depending on the source geometry, the two modes might not be excited equally. To determine the theoretical modal amplitudes, the method provided in section 2.5 is used. To simplify calculations, only the two propagating modes are used in the expansion. This may not be a good approximation as the piston source requires many more modes to properly recreate the initial condition at $z = 0$. However this approximation should still give a sense of the relative amplitudes of the two modes. Implementing the two mode expansion for a source radius of $a = 2.5$ cm and $\phi_0 = 1$ gives the modal amplitudes shown in table 5.1. Looking at the calculated amplitudes it clear that for this size of source both modes get excited at similar levels so it is unlikely that either ET0 or ET1 is being measured without the other.

As the theory suggests there should be two visible propagating modes, there must be various aspects of the physical system that do not allow for ideal sound propagation. Any deviations from an unbroken tube will affect propagation as was demonstrated by *Wilson et al.* (2003) and *Lenhart et al.* (2016). The pipe is assembled in discrete pieces to allow for the hydrophone input fittings. These solder joints could cause changes in the ideal propagation. Additionally, while the theory uses a circular piston as its source, the real source used is not as simple. It consists of a hydrophone element with a 2.5 cm tall cylinder as the piezoelectric component. This element will not behave as a plane source as is assumed but will have an associated beam pattern. Additionally since this element is taller than it is wide it is not projecting in an axisymmetric regime. All the previous theory has been done with the axisymmetric assumption as it can be solved analytically. However there exists a whole other class of modes that additionally can be supported. Due to the element geometry it is not unreasonable to assume these other modes are being excited and that is what is being detected in the group speed measurement. There has been little work done on the non-symmetrical modes as the associated equations become difficult to solve. Numerical studies exist such the work done by *Zemanek Jr* (1972) who uses numeric methods to characterize the system for the first 4 antisymmetric modes. Future

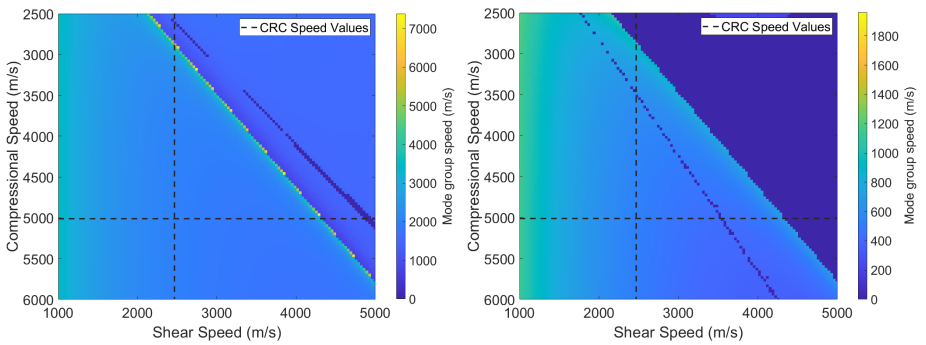

(a) ET0 (b) ET1

Figure 5.10: Modal speeds for the elastic waveguide at multiple (c_s,c_c) pairs

work should ensure that only symmetrical modes are propagating or a new model needs to be created to take into account the added complexity.

The source model is also inaccurate due to its assumption of single frequency tones for the propagation. The analysis assumes that the source is infinitely narrow which allows for only one propagation frequency. This is only correct in a steady state scenario where there is no time-dependence. If the source signal is time-limited a finite bandwidth signal packet will propagate and potentially undergo dispersion. This will decrease the effectiveness of the matched filter as the correlation between the received signal and the transmitted signal will be worse. In addition, the transmitted signals used for these calibrations are not single frequency tones but are small bandwidth linear sweeps which will also have associated dispersion. To account for this, the modal expansion needs to be performed for all frequencies in the sweep.

There is another aspect of the system that must be acknowledged. This work uses *Haynes* (2014) for physical constants of wall material. While an accepted source for material properties, in general there are unknowns associated with it. The precise type of copper used is unknown as the system was assembled many years before the start of the investigation. In particular, the compressional speed and shear speed can vary depending on the type of copper. To investigate how a variance in the wall material speed changes the predicted modes, the model was run multiple time for a range of compressional-shear speed pairs. This is shown in figure 5.10. For both modes while a change in material speeds causes changes in modal speeds, for any reasonable value for compressional or shear speed

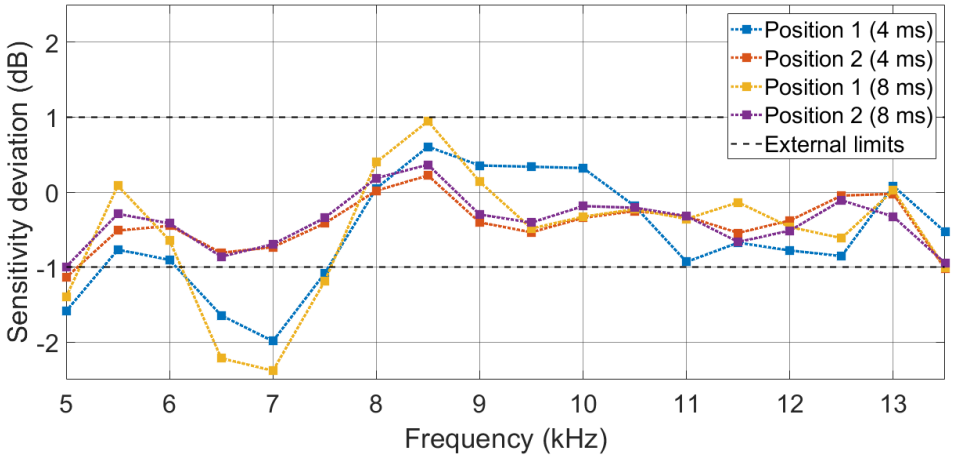

Figure 5.11: Deviation between measured sensitivity and external calibration

the modal speeds do not vary significantly. For this to be the cause of the magnitude deviation observed, nonphysical values of c_s and c_c would be required. Regardless, due to the inherent sensitivity of non-ideal tube geometry, a future system should be created with careful choice of material as well as minimizing any possible geometric deviations.

5.2 Sensitivity measurement

The measured sensitivity generally agrees with the external reference measurements performed by Teledyne Reson. Comparing the results from the two positions for both sweep lengths, the results from position 2 are consistently closer to the external measurement. This is the case despite the dispersion measurement in position 2 having more null points as shown in figure 5.1. Figure 5.11 shows that the deviation from the measured sensitivity is as high as -2.5 dB at 7 kHz. The deviation also suggests that the external calibration is higher than reality since the measurements are generally below the Reson data. As the calculated sensitivity is based on the external value through the reference sensitivity with equations 3.18 and 3.19, an overestimate of the sensitivity values would double their effect on the calibration result so that even a small deviation would be noticeable. It is not unreasonable for the Reson values to be an underestimate as the external calibrations were performed in October 2020. Long-term loss of hydrophone sensitivity is still a poorly studied topic for research, however it has been observed than an aging ceramic causes decrease in sensitivity on the order of dB/year (*Andrew et al.*, 2011). Anecdotal evidence

from Ocean Sonic's customers has confirmed that the RB9 sensors experience a small decrease in their sensitivity over time which could explain the consistent underestimation of the measured calibration compared to the external data. In addition, the Reson data is only the sensitivity of the element alone and does not consider the other analog and digital components in the hydrophones that may affect the sensitivity. The icListen hydrophones also contain a pre-amplifier and analog to digital converter (ADC) which have their own sensitivity effects. These have not been studied in great detail but generally they do not affect the sensitivity by more than 1 dB. By performing a more recent calibration on these units that takes into account the entire analog data flow a more accurate value for sensitivity can be used to qualify the measurements.

As previously mentioned, though the measurements generally agree with the external measurement, there is a large difference between the measurements done in position 1 and position 2. As the system electronics and processing did not change between the two measurements it stands to reason that the difference is due to the positions themselves and not measurement errors. Assuming the Reson sensitivities are correct, both hydrophones should measure the same received pressure (calculated using the provided sensitivities) in their respected positions. These received pressures for all four measurements are shown in figure 5.12. Comparing the received pressure in both positions, it is clear that the most variation in sensitivity per figure 5.11 are in regions that have high spread in the received pressure. This is shown further in figure 5.13 where the greatest differences in pressure are at 6.5 - 7.5 kHz and 8.5 - 9.5 kHz.

The question becomes what is causing a large difference in pressure in position 1 that is not present in the position 2 measurements. As there is no significant decrease in pressure in the regions of interest, this decrease is likely not a measurement error due to low signal to noise ratio. Additionally, as the received pressure is generally lower in position 2 it is unlikely that the variation seen in position 1 is caused by high noise in the system. Due to the inherent variability of making acoustic measurements it is possible that this is due to small changes in the coupling. The hydrophones are not suspended in free-space and have to be coupled into the system through acetyl collars. This coupling introduces potential variance as vibrations in the hydrophone can induce a change in measured pressure. The degree in which the collar can couple to the position 1 opening versus the position 2

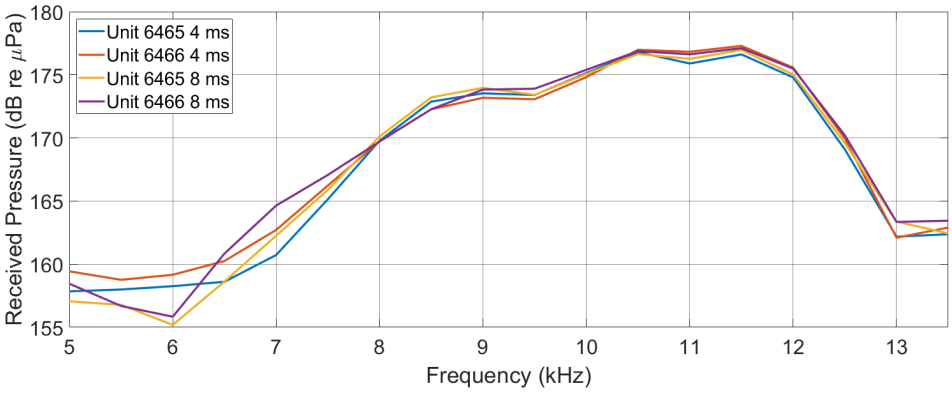

(a) Position 1

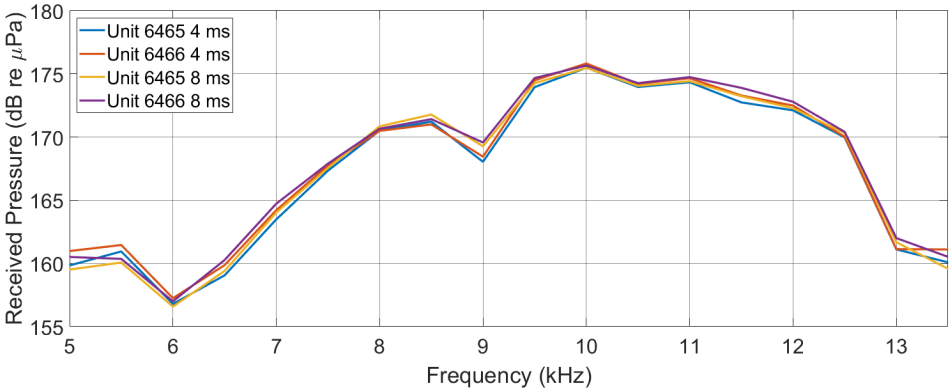

(b) Position 2

Figure 5.12: Measured received pressure level (dBμPa) from the normalized matched filter

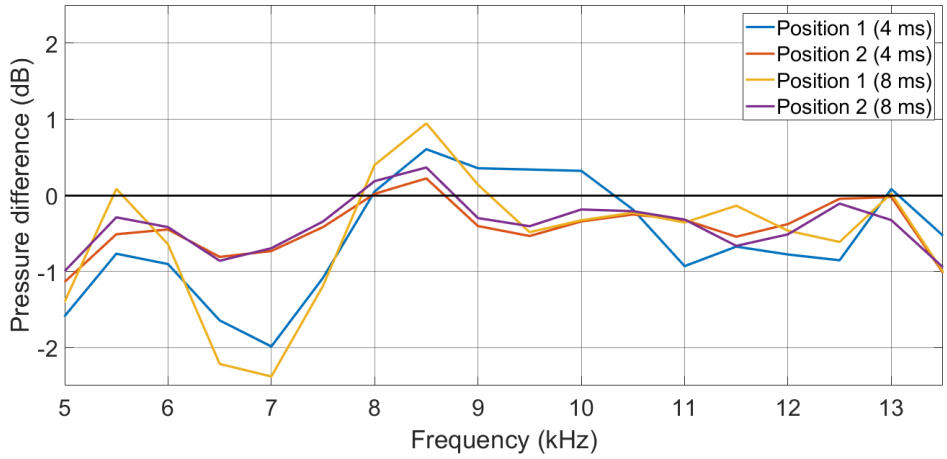

Figure 5.13: Difference in measured pressure between the unit under test and the reference hydrophone for all for measurements

opening could possibly explain the variance in the pressure measurements. Coupling variance could also be introduced due to the nature of how the system is shaped. The openings for the projector and position 1 are mechanically connected and isolated by a foam separator. This is not the case between the projector and position 2. Additionally, the two openings are not at the same height, this causes the water levels to be unequal. While the water level should be enough for the entire sensing element to be submerged there is a possibility that this variance could also cause pressure variability.

Due to all the intrinsic variability in the measurement system, it is generally not possible to give a single reason for why the pressure measurements have deviations. However, as shown by the corresponding calibration measurements, even with two year old sensitivity references, these deviations are not large except at particular frequency ranges therefore sensitivity measurements can be performed to acceptable accuracy for much of the measurement band.

5.3 Recommendations for future work

Future work on this topic is recommended to better understand the unknowns presented in the previous sections. The measured data shows that the results do not agree with the predicted modes from *Del Grosso* (1968)'s analysis.

How the curvature affects the dispersion is not well studied and warrants further investigation. Without comparing to a straight pipe of similar diameter and material is not possible to experimentally show the effect. It is recommended that a second system be built using a length of straight pipe to independently verify the model. Multiple authors have shown that the elastic waveguide model presented by *Del Grosso* (1968) is experimentally verifiable (*Lafleur and Shields*, 1995; *Wilson et al.*, 2003). Performing the same work on a straight pipe would decouple the curved pipe effect from the waveguide and allow the model to be tested. A full numeric treatment of the elastic curved pipe would also be needed to fully characterize the system.

As discussed in section 5.1.3 the shear modulus of the pipe material is generally not well known. By simplifying the system to a straight segment that is controllable in length and diameter, the phase speed can be measured through standing wave patterns and used

to experimentally calculate the shear modulus and shear speed in the pipe material. With a better estimate of the material properties as well as better measurements of the geometry of the system the exact model prediction from *Del Grosso* (1968) can by found and compared to what is being measured in a curved system. Additionally the straight pipe should be measured by laser-Doppler vibrometry to detect the exact location of the highs and lows in pressure to aid in identification of modes.

A limitation the current work is the variation that has been introduced in the physical system itself such as the mounting points, uneven joins, and variable coupling. A new version of the curved system should be created with attention to the manufacturing detail to minimize the variability. This new system should also have a wider pipe diameter to accommodate larger sensors for calibration. Ideally, the ports for the hydrophones should be placed at distances from the projector calculated to have the fewest null effects based on the Doppler vibrometry results. The ports should be included only after the unobstructed pipe has been characterized through the standing waves.

It is also suggested that work be done to better qualify the source characteristics. As discussed in section 5.1.3, the projector used cannot be considered an axisymmetric source and the possibilities of non-symmetric propagating modes should be investigated. Additionally, it is recommended to attempt calibration using short clicks rather than sweeps to minimize potential dispersion of the wave packet due to the sweep bandwidth. Any finite-time signal will have dispersion so how time-limited signals integrate into the model should also be analyzed.

CHAPTER 6

CONCLUSION

In order to address the gaps in calibration measurement faced by many users, a novel system has been developed and tested to calibrate hydrophones below 10 kHz. This was done by utilizing the decreased sound speed that occurs when sound is propagating in a water-filled metal pipe known as the elastic waveguide effect. Continuing the work done by *Johnson and Garrett* (1985), this research presents a historical and theoretical background for the elastic waveguide as well as performs calibrated measurements on units of known sensitivity to qualify the system's effectiveness.

The calibration measurements show that there are still several unknowns in the physical system which cause deviations both in the measured group speed and the measured sensitivity. Many of these deviations are shown to be due the non-ideal nature of the system, such as the pipe's intrinsic curvature and the positions of the hydrophone collars and pipe clamps. Discussion of how these traits affect the measurements as well as suggested techniques for minimizing this in future work are provided.

Despite the deviations from the theorical wave propagation, this research shows that calibration within the 5 - 13.5 kHz band is both accurate to within 1 dB and repeatable across multiple measurements with the exception of 6.5 - 7.5 kHz measurements done in hydrophone position 1. The original work done by *Johnson and Garrett* (1985) using reciprocity had a systemic bias of 1.5 dB in their measurment of hydrophone sensitivity. This research improves upon these methods and demonstrates that using elastic waveguides is both an effective and simple method for low-frequency calibration.

BIBLIOGRAPHY

Andrew, R. K., B. M. Howe, and J. A. Mercer, Long-time trends in ship traffic noise for four sites off the north american west coast, *The Journal of the Acoustical Society of America*, *129*, 642–651, 2011.

Bansevičius, R., and V. Kargaudas, Wave propagation in rigid cylindrical tubes with viscous and heat-conducting fluid, *Ultragarsas/Ultrasound*, *56*, 7–10, 2005.

Benade, A. H., On the propagation of sound waves in a cylindrical conduit, *The Journal of the Acoustical Society of America*, *44*, 616–623, 1968.

Bobber, R. J., General reciprocity parameter, *The Journal of the Acoustical Society of America*, *39*, 680–687, 1966.

Bobber, R. J., and G. A. Sabin, Cylindrical wave reciprocity parameter, *The Journal of the Acoustical Society of America*, *33*, 446–451, 1961.

Chow, J. C., and J. T. Apter, Wave propagation in a viscous incompressible fluid contained in flexible viscoelastic tubes, *The Journal of the Acoustical Society of America*, *44*, 437–443, 1968.

Cochran, J. A., Remarks on the zeros of cross-product bessel functions, *Journal of the Society for Industrial and Applied Mathematics*, *12*, 580–587, 1964.

Dakin, D. T., N. Bailly, J. Dorocicz, and J. Bosma, Calibrating hydrophones at very low frequencies, in *Proceedings of the 2nd International Conference and Exhibition on Underwater Acoustics*, pp. 373–378, 2014.

Daniels, F. B., On the propagation of sound waves in a cylindrical conduit, *The Journal of the Acoustical Society of America*, *22*, 563–564, 1950.

Del Grosso, V. A., Systematic errors in ultrasonic propagation parameter measurements. part 1: Effect of freefield diffraction, *Tech. rep.*, Naval Research Lab Washington DC United States, 1964.

Del Grosso, V. A., Systematic errors in ultrasonic propagation parameter measurements. part 2. effect of guided cylindrial modes, *Tech. rep.*, Naval Research Lab Washington DC United States, 1965.

Del Grosso, V. A., Systematic errors in ultrasonic propagation parameter measurements. part 4: Effect of finite thickness elastic solid tubes enclosing the liquid cylinder of interest, *Tech. rep.*, Naval Research Lab Washington DC United States, 1968.

Del Grosso, V. A., Analysis of multimode acoustic propagation in liquid cylinders with realistic boundary conditions–application to sound speed and absorption measurements, *Acta Acustica united with Acustica*, *24*, 299–311, 1971.

Del Grosso, V. A., and R. E. McGill, Remarks on axially symmetric vibrations of a thin cylindrical elastic shell filled with non viscous compressible fluid, *Acustica*, *20*, 313, 1968.

Del Grosso, V. A., and R. E. McGill, Sound-speed dispersion in liquid cylinders, *The Journal of the Acoustical Society of America*, *48*, 1294–1296, 1970.

Elvira-Segura, L., Acoustic wave dispersion in a cylindrical elastic tube filled with a viscous liquid, *Ultrasonics*, *37*, 537–547, 2000.

Fuller, C., and F. J. Fahy, Characteristics of wave propagation and energy distributions in cylindrical elastic shells filled with fluid, *Journal of Sound and Vibration*, *81*, 501–518, 1982.

Gazis, D. C., Three-dimensional investigation of the propagation of waves in hollow circular cylinders. i. analytical foundation, *The Journal of the Acoustical Society of America*, *31*, 568–573, 1959.

Golenkov, A., and Y. G. Rachkov, Hydrophone calibration at low frequency under elevated hydrostatic pressures, *Measurement Techniques*, *23*, 942–947, 1980.

Greenspon, J. E., and E. Singer, Propagation in fluids inside thick viscoelastic cylinders, *The Journal of the Acoustical Society of America*, *97*, 3502–3509, 1995.

Haynes, W., *CRC Handbook of Chemistry and Physics*, CRC Handbook of Chemistry and Physics, CRC Press, 2014.

IEC 60565-1:2020, IEC 60565-1:2020 Underwater acoustics - Hydrophones - Calibration of hydrophones - Part 1: Procedures for free-field calibration of hydrophones, *Standard*, International Electrotechincal Commission, Geneva, CH, 2020.

Johnson, M. B., and S. L. Garrett, Reciprocity calibration in a compliant cylindrical tube, *The Journal of the Acoustical Society of America*, *78*, S54–S54, 1985.

Joubert, C., G. Nolet, A. Sukhovich, A. Oge, J.-F. Argentino, and Y. Hello, Hydrophone calibration at very low frequencies, *Bulletin of the Seismological Society of America*, *105*, 1797–1802, 2015.

Keefe, D. H., Acoustical wave propagation in cylindrical ducts: Transmission line parameter approximations for isothermal and nonisothermal boundary conditions, *The Journal of the Acoustical Society of America*, *75*, 58–62, 1984.

Kirchhoff, G., On the influence of heat conduction in a gas on sound propagation, *Annual Review of Physical Chemistry*, *134*, 177–193, 1868.

Klip, W., P. Van Loon, and D. A. Klip, Formulas for phase velocity and damping of longitudinal waves in thick-walled viscoelastic tubes, *Journal of Applied Physics*, *38*, 3745–3755, 1967.

Kwun, H., K. A. Bartels, and C. Dynes, Dispersion of longitudinal waves propagating in liquid-filled cylindrical shells, *The Journal of the Acoustical Society of America*, *105*, 2601–2611, 1999.

Lafleur, L. D., and F. D. Shields, Low-frequency propagation modes in a liquid-filled elastic tube waveguide, *The Journal of the Acoustical Society of America*, *97*, 1435–1445, 1995.

Lenhart, R. D., J. D. Sagers, and P. S. Wilson, Development of a standing wave apparatus for calibrating acoustic vector sensors and hydrophones, *The Journal of the Acoustical Society of America*, *139*, 176–187, 2016.

Lin, T., and G. Morgan, Wave propagation through fluid contained in a cylindrical, elastic shell, *The Journal of the Acoustical Society of America*, *28*, 1165–1176, 1956.

MacLean, W. R., Absolute measurement of sound without a primary standard, *The Journal of the Acoustical Society of America*, *12*, 140–146, 1940.

Moon, P., and D. E. Spencer, Separability in a class of coordinate systems, *Journal of the Franklin Institute*, *254*, 227–242, 1952.

Morgan, G., and J. Kiely, Wave propagation in a viscous liquid contained in a flexible tube, *The Journal of the Acoustical Society of America*, *26*, 323–328, 1954.

Morse, P. M., The transmission of sound inside pipes, *The Journal of the Acoustical Society of America*, *11*, 205–210, 1939.

Peterson, E. W., Acoustic wave propagation along a fluid-filled cylinder, *Journal of Applied Physics*, *45*, 3340–3350, 1974.

Plona, T. J., B. K. Sinha, S. Kostek, and S.-K. Chang, Axisymmetric wave propagation in fluid-loaded cylindrical shells. ii: Theory versus experiment, *The Journal of the Acoustical Society of America*, *92*, 1144–1155, 1992.

Prek, M., Analysis of wave propagation in fluid-filled viscoelastic pipes, *Mechanical Systems and Signal Processing*, *21*, 1907–1916, 2007.

Rama Rao, V., and J. Vandiver, Acoustics of fluid-filled boreholes with pipe: Guided propagation and radiation, *The Journal of the Acoustical Society of America*, *105*, 3057–3066, 1999.

Rossing, T. D., and N. H. Fletcher, *Principles of vibration and sound*, chap. 8, Springer, New York, 2004.

Rubinow, S., and J. B. Keller, Wave propagation in a fluid-filled tube, *The Journal of the Acoustical Society of America*, *50*, 198–223, 1971.

Schloss, F., and M. Strasberg, Hydrophone calibration in a vibrating column of liquid, *The Journal of the Acoustical Society of America*, *34*, 958–960, 1962.

Sinha, B. K., T. J. Plona, S. Kostek, and S.-K. Chang, Axisymmetric wave propagation in fluid-loaded cylindrical shells. i: Theory, *The Journal of the Acoustical Society of America*, *92*, 1132–1143, 1992.

Stokes, G. G., On the theories of internal friction of fluids in motion, *Transactions of the Camberidge Philosophical Society*, *8*, 287–305, 1845.

von Helmholtz, H., On the influence of friction in the air on sound motion, *Verhandl. Naturhist. Med. Ver. Heidelberg*, *3*, 16–20, 1863.

Wilson, P. S., R. A. Roy, and W. M. Carey, An improved water-filled impedance tube, *The Journal of the Acoustical Society of America*, *113*, 3245–3252, 2003.

Zemanek Jr, J., An experimental and theoretical investigation of elastic wave propagation in a cylinder, *The Journal of the Acoustical Society of America*, *51*, 265–283, 1972.